University of Alberta

The Use of Megavoltage Computed Tomography for Treatment Planning of Patients with Prostate Cancer and Metal Hip Prostheses

by 

David Kiyoshi Sasaki

A thesis submitted to the Faculty of Graduate Studies and Research
in partial fulfillment of the requirements for the degree of

Master of Science
in
Medical Physics

Department of Physics

Edmonton, Alberta
Spring 2008

Library and Archives Canada

Published Heritage Branch

395 Wellington Street
Ottawa ON K1A 0N4
Canada

Bibliothèque et Archives Canada

Direction du Patrimoine de l'édition

395, rue Wellington
Ottawa ON K1A 0N4
Canada

Your file Votre référence
ISBN: 978-0-494-45881-5
Our file Notre référence
ISBN: 978-0-494-45881-5

NOTICE:
The author has granted a non-exclusive license allowing Library and Archives Canada to reproduce, publish, archive, preserve, conserve, communicate to the public by telecommunication or on the Internet, loan, distribute and sell theses worldwide, for commercial or non-commercial purposes, in microform, paper, electronic and/or any other formats.

The author retains copyright ownership and moral rights in this thesis. Neither the thesis nor substantial extracts from it may be printed or otherwise reproduced without the author's permission.

AVIS:
L'auteur a accordé une licence non exclusive permettant à la Bibliothèque et Archives Canada de reproduire, publier, archiver, sauvegarder, conserver, transmettre au public par télécommunication ou par l'Internet, prêter, distribuer et vendre des thèses partout dans le monde, à des fins commerciales ou autres, sur support microforme, papier, électronique et/ou autres formats.

L'auteur conserve la propriété du droit d'auteur et des droits moraux qui protège cette thèse. Ni la thèse ni des extraits substantiels de celle-ci ne doivent être imprimés ou autrement reproduits sans son autorisation.

In compliance with the Canadian Privacy Act some supporting forms may have been removed from this thesis.

While these forms may be included in the document page count, their removal does not represent any loss of content from the thesis.

Conformément à la loi canadienne sur la protection de la vie privée, quelques formulaires secondaires ont été enlevés de cette thèse.

Bien que ces formulaires aient inclus dans la pagination, il n'y aura aucun contenu manquant.

Canada

Abstract

We have used megavoltage CT (MVCT) images to overcome difficulties produced by metal artifacts within kilovoltage CT (kVCT) images of prostate cancer patients with hip prostheses. This investigation included measurement of the MVCT number-to-electron density curve, comparison of MVCT and kVCT images for delineation and dose calculations and assessment of the accuracy of the Varian Anisotropic Analytical Algorithm (AAA) in calculating dose distributions in the presence of metal. We have found that MVCT images can be reliably calibrated, and that there is some clinical advantage in using MVCT images for target delineation. Comparisons of kVCT and MVCT images for dose calculation revealed differences of only 1.4% of the prescribed dose behind a hip prosthesis however. Comparisons of measurements to AAA calculations revealed that the AAA algorithm overestimates dose behind a steel rod by 10% to 20%.

Table of Contents

Index of Tables

Illustration Index

Chapter 1: Thesis Overview

1.1 Thesis Overview

In modern radiotherapy treatment planning, the information in diagnostic computed tomography (CT) images is used to delineate regions of interest and to provide an electron density map used to calculate dose distributions. In prostate cancer patients with hip prostheses, the implants produce artifacts in diagnostic CT images such that the locations of regions of interest and accurate electron densities are difficult to obtain. The filtered backprojection algorithm used to reconstruct CT images assumes that the projection-backprojection process is linear, which is a good enough assumption for imaging of normal body tissues to produce images that are "almost photographically perfect" [1]. In the filtered backprojection of metal, nonlinearities such as beam hardening and photon starvation undermine this assumption.

We have used megavoltage CT (MVCT) images for treatment planning in an attempt to overcome these problems, as the higher energy of the photons of the beam helps prevent photon starvation. Beam hardening, the preferential attenuation of lower energy photons in a polyenergetic beam, is also lessened because the photons of a 3.5 MV beam interact almost exclusively through Compton or incoherent scattering and the total attenuation coefficient is less strongly dependent on energy than for kVCT energies. The MV beam is generated by a linear accelerator, as opposed to an x-ray tube as used in kilovoltage CT (kVCT).

The investigation was done in three different sets of experiments. The first was a calibration of the megavoltage CT number-to-electron density curve and an investigation into the accuracy of MVCT and kVCT numbers in the presence of metal. The second was an investigation of the clinical advantage of using MVCT versus kVCT images for target delineation and dose calculations. The final set of measurements assessed the accuracy of the Varian AAA dose calculation algorithm in calculating dose distributions in a water phantom containing a steel rod. The three experiments together attempt to show that MVCT images may be used in treatment planning and assess any

advantage that MVCT offers for planning prostate cancer patients with hip prostheses.

Since the work described in this thesis was carried out in three separate, semi-independent sets of experiments, the thesis is therefore laid out in the three components, each with its own objective, theory, methods and materials, and results and discussion. The main body of work is preceded by a project overview and introduction, and is followed by a discussion and final conclusions, each constituting a separate chapter.

1.2 Chapter Overviews

Chapter 2 provides a background of concepts important to this work. This includes a discussion of cancer and its treatments, focusing on cancer of the prostate and external beam radiotherapy. The treatment planning process is outlined in general, followed by a more in-depth discussion of how the presence of hip prostheses interferes with this process. Megavoltage computed tomography is introduced as a possible solution to the treatment planning complications introduced by the presence of metal hip prostheses in patients with prostate cancer.

Chapter 3 describes the measurements used to measure the MVCT number-to-electron density calibration curve. The images used for this measurement were also used to assess the impact of metal artifacts on both MVCT and diagnostic CT (kVCT) images.

Chapter 4 describes the comparison made between MVCT and kVCT images for delineating the prostate when metal hip prostheses are present. Also described are the comparisons made between treatment planning calculations carried out using kVCT images and those carried out using MVCT images of patients with metal hip prostheses.

Chapter 5 describes the comparison of dose measurements in a water phantom to treatment plans generated using MVCT scans of the phantom with both the commercial treatment planning system in use in our clinic and Monte Carlo simulations. The comparison afforded an assessment of the accuracy of our clinical treatment planning system in the presence of metal objects.

Chapter 6 discusses the results of the three previous chapters, and evaluates their impact

on the overall project. Final conclusions regarding the findings of this thesis are summarized, along with a final appraisal of the clinical viability of this work.

Chapter 2: Introduction

2.1 Cancer

Cancer is a term used to describe a number of diseases and is defined by Webster's dictionary to be: "A malignant tumour that invades healthy tissue and spreads to other areas" or "the disease marked by such tumours" [2]. The various types of cancer are always named for the site of the body in which they originate (ie brain cancer, liver cancer, etc.). They can be further distinguished by the type of cell that forms the tumour, and therefore there is more than one type of cancer that can grow in each organ. A brain tumour involving the glial cells for example is called a glioma, while a tumour involving the cells of the meninges is called a meningioma.

Though there are many different types of cancer, with vastly different growth rates, mortality rates and treatments, they are all caused by abnormalities in the behaviour of cells in the body. Normally genes inside each cell govern the growth, function, reproduction and termination of the cell in the interest of the larger body of which the cell forms a part. When these processes are governed properly, the cell is a working member of a larger group of cells carrying out some function for the body [3]. Tumours form when these processes, especially reproduction and termination, are no longer controlled properly and a group of cells is formed which no longer acts in the interests of the body. These groups are called tumours and are classified as either benign or malignant. Benign tumours stay in one place and are generally not life-threatening. Malignant tumours will spread from their original site to infest other areas of the body, and if left unchecked will eventually impede the function of a critical organ, causing death.

Cancer is currently the second most fatal chronic disease after cardiovascular disease [4], and is the "leading cause of premature death – or early death – in Canada" [5]. It is estimated that there will be 159,900 new cases of cancer and 72,200 deaths resulting

from cancer in Canada in 2007 [6]. Based on the current rate of incidence of cancer, 39% of Canadian women and 44% of men will develop cancer during their lifetimes [6]. Approximately 24% of women and 28% of men in Canada will die of the disease. The percentage distribution of estimated new cases and deaths for selected cancers in 2007 for Canadian males and females can be seen in Figure 2.1 and Figure 2.2 respectively.

2.2 Treatment of Cancer

The three most common treatments for cancer are surgery, radiotherapy and chemotherapy. Other less common forms of treatment include hormonal therapy and stem cell transplant and are given in certain instances for some types of cancer [7]. The goal of treatment depends upon many factors, including the type of cancer, the progress of the disease and the health of the patient. The goal can be the prevention of the growth of cancer cells or the removal of precancerous tissue, cure of existing disease, control of existing disease, or palliation when cure is not possible.

Oncologists will decide which form of treatment is best, and what the goal of the treatment should be. Different forms of treatment may be combined and administered either concurrently or successively. All treatments fall into one of two categories: they are either local or systemic. Local treatments are those procedures designed to affect a localized region of the body. Surgery would be an example of a local treatment. Systemic treatments are designed to reach cells throughout the entire body, and generally travel through the blood stream. They are usually used for cancers which have spread to multiple sites in the body. Many chemotherapy treatments are systemic [7].

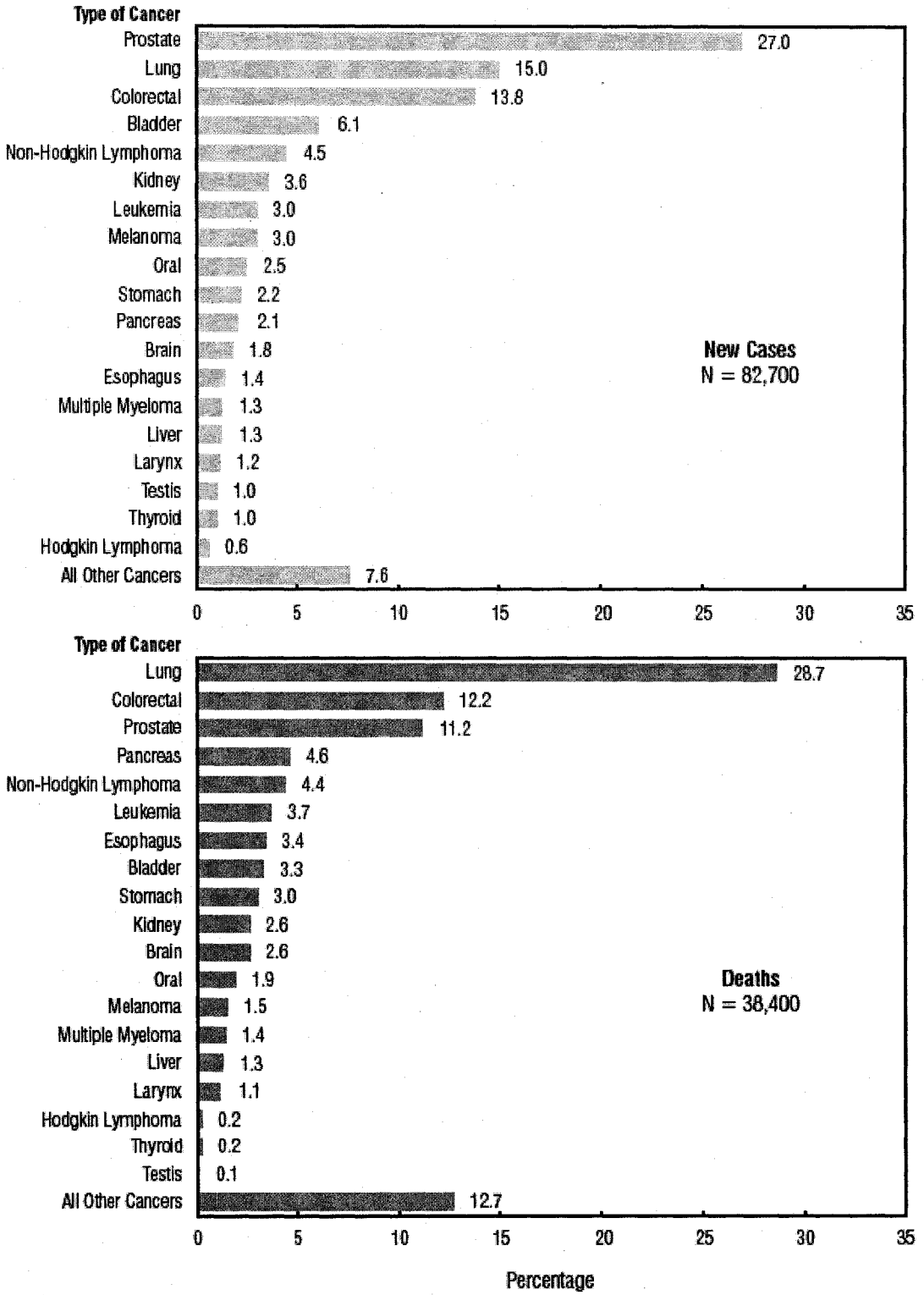

Figure 2.1: Percentage distribution of estimated new cases and deaths for selected cancers, males, Canada, 2007 [6].

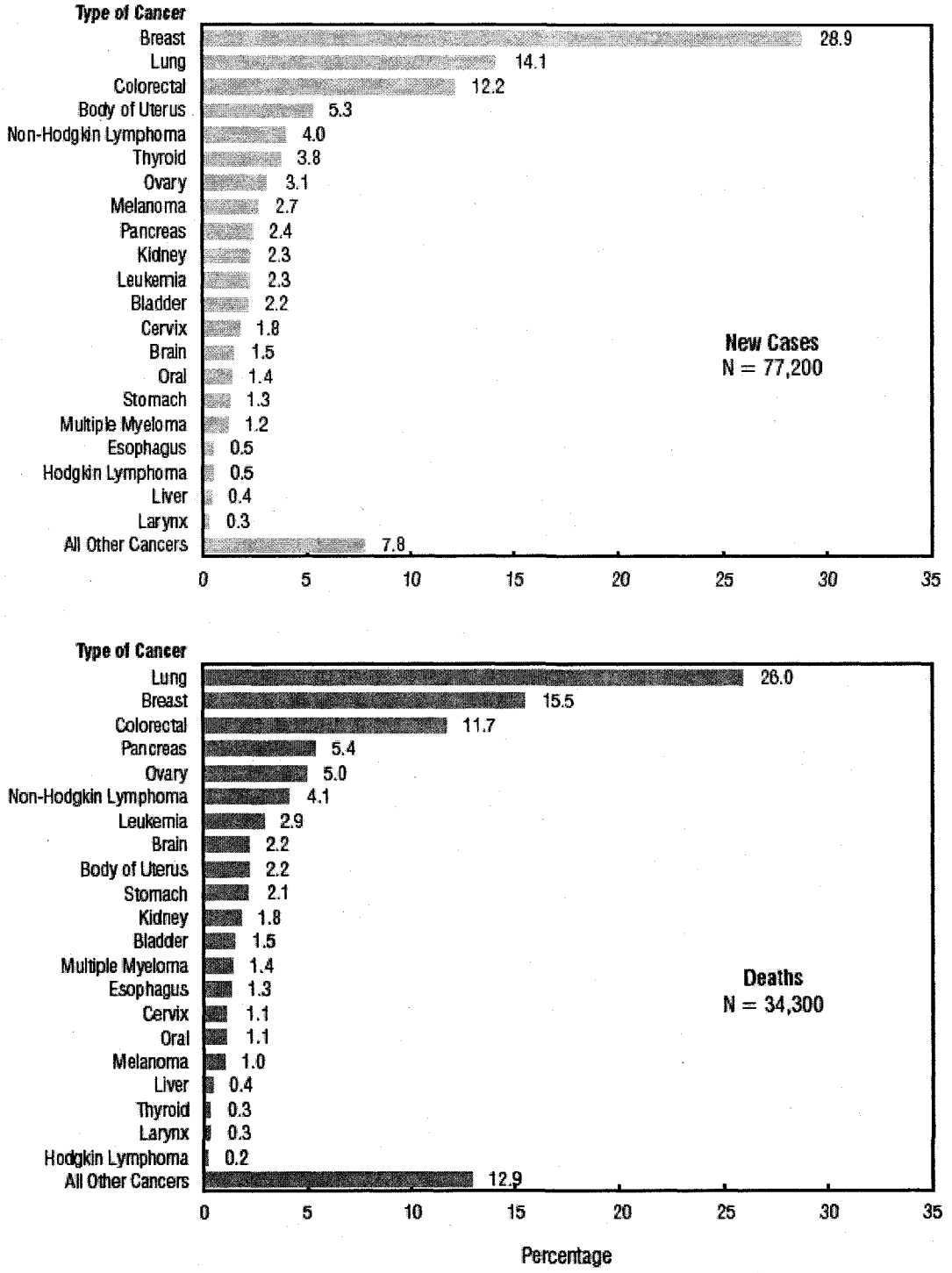

Figure 2.2: Percentage distribution of estimated new cases and deaths for selected cancers, females, Canada, 2007 [6].

2.3 External Beam Radiation Therapy

In external beam radiation therapy, linear accelerators are used to produce beams of radiation which are directed at the tumour from various angles to reduce the amount of radiation absorbed by healthy tissues surrounding the target. A linear accelerator can be seen in Figure 2.3 [8]. It can be used alone as a curative treatment, after surgery to kill any remaining microscopic disease, or for palliative purposes in advanced cases. The radiation is usually delivered once a day for 6 to 8 weeks [7]. This is done to exploit the inability of cancerous tissue to repair radiation damage, giving healthy tissue a chance to recover to reduce harmful side effects and/or increase the dose delivered to the tumour. Radiation dose is measured in gray (Gy) and is defined as the energy deposited by ionizing radiation per unit mass of material. One gray is equal to one joule per kilogram.

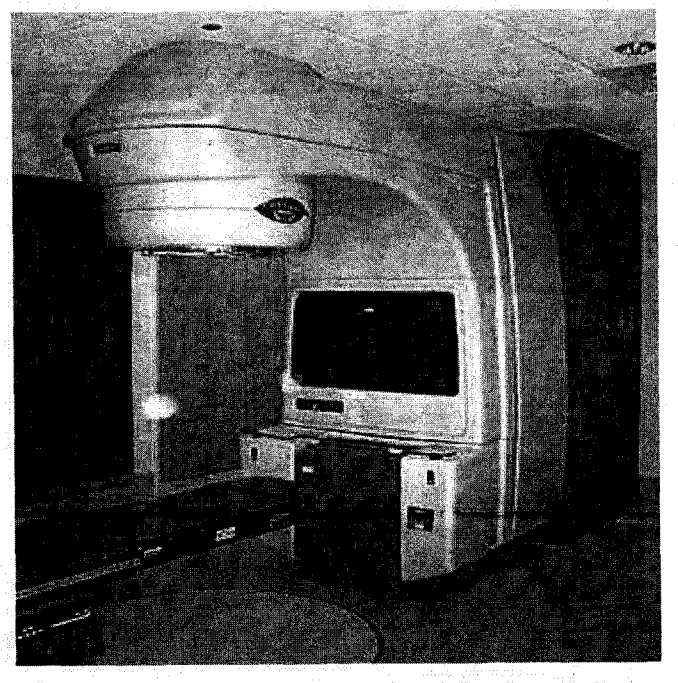

Figure 2.3: A linear accelerator [8].

Radiotherapy has evolved since its beginnings and now includes four different types of external beam treatments: conventional delivery, three dimensional conformal radiotherapy (3DCRT), intensity-modulated radiotherapy (IMRT) and image guided adaptive radiotherapy (IGAR). Conventional delivery involves the use of rectangular fields of radiation, possibly with simple beam blocking, for treatment of cancer. In many cases, it is no longer the standard today. This method irradiates more healthy tissue than methods used currently, as limited imaging capabilities made it impossible in the past to resolve the locations of disease and critical structures accurately. 3DCRT came into widespread use once 3D imaging modalities (CT, MR, etc.) improved, and allowed for detailed spatial information to be entered into the planning process. With improved knowledge of the positions of all critical structures, the beams could be shaped to conform to the tumour with a margin added to account for organ motion and setup error. This tightening of the dose distribution helps spare organs at risk. In this way, the dose given to the tumour can be escalated without increasing damage to healthy tissue. IMRT can be viewed as a more advanced form of 3DCRT. 3DCRT involves geometrical shaping of the field only, and therefore involves only two intensity regions in a given field: high and low. IMRT takes 3DCRT one step further and modulates the intensity of the field so that there is a number of intensity regions. This makes it possible to create complicated isodose surfaces, including concave surfaces, which are extremely difficult to create with 3DCRT. IGAR incorporates all of the advances of IMRT and adds CT imaging before or during the delivery of each fraction, permitting the treatment to be adjusted on a fraction-to-fraction basis to account for organ motion and changes in patient geometry over the course of the treatment. This allows planners to tighten the dose distribution around the tumour further, since the fraction to fraction uncertainty regarding the location of the tumour and surrounding critical structures is eliminated.

2.3.1 Overview of the Treatment Planning Process

The treatment planning process begins with a 3D CT scan of the region of interest, but may also include MRI, PET, SPECT, etc. Immobilization devices are often constructed

for this scan and used when delivering each fraction of radiation. These are often moulds made of rigid plastic, and can be fixed to the treatment couch in order to constrain movement. Since the radiation is given once a day for several weeks, the patient will not be in exactly the same position for each fraction. The goal of the immobilization device is to ensure that this setup variation is as small as possible. The scan or scans are then transferred to a treatment planning station where physicians and planners use them to delineate all structures of interest, including organs at risk and the tumour itself. At this stage, depending on the location of the tumour, size of the patient, and locations of organs at risk, the energy of the radiation to be used, the size of the radiation field, and the direction of the fields to be used are chosen. These will be referred to as beams. Any blocks, or beam modifiers needed to shield organs at risk are also added to the plan. Once beams have been applied to the CT scan of the patient, the treatment planning system can make use of the CT numbers in the images, which can be related to the electron density of the tissues they represent, to calculate the dose distribution resulting from a given beam arrangement. A suitable beam arrangement is then chosen which will deliver adequate dose to the tumour and keep the dose to organs at risk below their tolerance levels. This stage is important, and central to this thesis. If the CT numbers themselves, the conversion curve used to convert them into electron densities, or the dose calculation algorithm is inaccurate, then proper assessment of a treatment plan is difficult or impossible. In the treatment of a prostate patient with hip prostheses, the CT numbers, their translation into densities for calculation, and the dose calculation algorithm are all suspect.

If a treatment plan is acceptable, it is transferred to the treatment delivery station where it is used for delivering the treatment. If it is unacceptable, the beam arrangement can be modified until it becomes acceptable.

2.4 Prostate Cancer

The prostate is a small, chestnut-shaped organ and is part of the reproductive and urinary systems of men. A diagram showing the prostate and the surrounding anatomy can be seen in Figure 2.4 [7]. Figure 2.5 shows the critical structures surrounding the

prostate for a patient with bilateral hip prostheses.

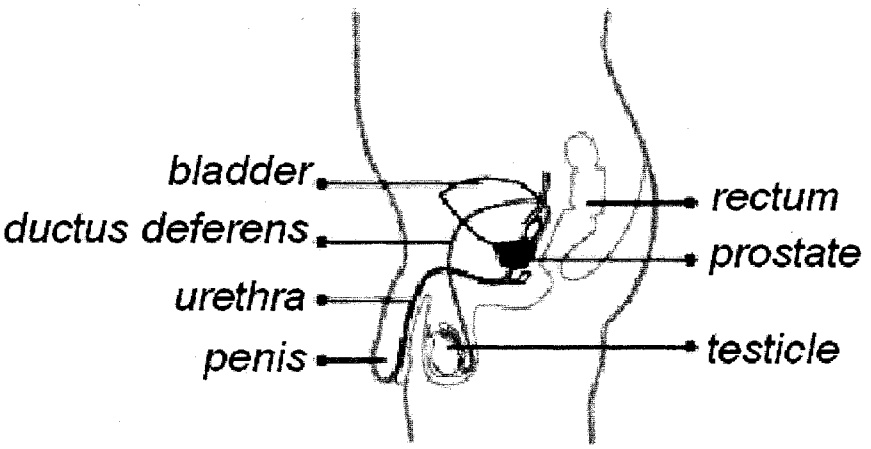

Figure 2.4: Illustration of the prostate and surrounding anatomy.

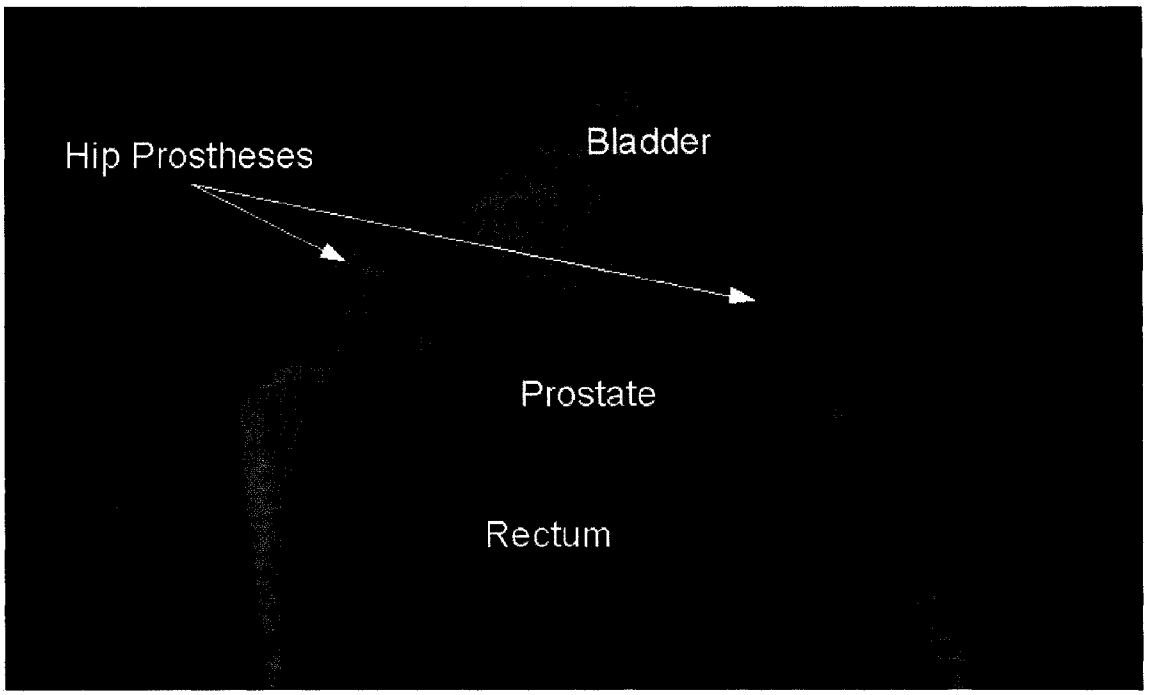

Figure 2.5: A 3D CT reconstruction of the critical structures surrounding the prostate.

It is estimated that there will be 22,300 new cases of prostate cancer in Canada in 2007 [7]. Prostate cancer is the most commonly diagnosed cancer in Canadian men.

Approximately 95% of prostate cancers are adenocarcinomas. Other rarer types of tumours which can occur in the prostate are: transitional cell carcinoma, sarcomas, small cell (neuroendocrine) carcinoma and ductal, mucinous and large duct tumours [7]. Prostate cancer often spreads to nearby organs, including the bladder, urethra and rectum. It may also spread to the lymph nodes surrounding the prostate and other more distant parts of the body, the most common being bone in the back, thighs, hips, or neck [7].

2.4.1 Treatment of Prostate Cancer

There are five categories of treatments that are used in fighting prostate cancer: watchful waiting, surgery, hormonal therapy, chemotherapy and radiotherapy. Watchful waiting entails careful monitoring of the progress of the disease with no direct intervention. This is an option for those with a low or intermediate grade prostate cancer that is confined to the prostate, those who are elderly and have other health concerns, those who have a life expectancy of less than 10 years, or those who prefer not to have treatment to avoid side effects. Surgery can entail possible cure of the cancer by complete removal of the disease, or relieving symptoms of an enlarged prostate through the removal of prostate tissue. Hormonal therapy is a systemic therapy which involves changing hormone levels of the body through surgery, drugs or radiotherapy to slow the growth and spread of cancer cells. It is not a cure. Chemotherapy is a systemic therapy involving the circulation of cytotoxic drugs throughout the body to kill cancerous cells. Chemotherapy may be used for palliation of cancers that are resistant to hormone therapy. Radiation therapy is the final method of treating prostate cancer, and comes in three different varieties: brachytherapy, unsealed radioactive isotope therapy, and external beam radiotherapy. Brachytherapy is the use of sealed radioactive sources placed near or inside the prostate using needles or catheters. Unsealed radioactive isotopes are used in solutions and are administered as systemic treatments. They are used for palliation purposes in patients with advanced cancers that have spread to multiple sites. External beam radiotherapy involves the use of a linear accelerator (linac) to produce a beam of ionising radiation which can be directed at the prostate

from outside the body [7].

2.5 External Beam Radiation Therapy for Prostate Cancer

Cancer of the prostate is usually treated with external beam radiotherapy [7]. The prostate, the seminal vesicles and the lymph nodes may all be irradiated depending on the stage of the cancer. Critical structures which must be avoided in external beam prostate treatments are the bladder, the rectum, and the urethra. The most common beam arrangement in conventional and conformal radiotherapy used for treating the prostate is the four field box, and is shown in Figure 2.6. This technique is widely used because it allows for a fairly uniform dose to the prostate without over-irradiating the bladder or the rectum, located anterior and posterior to the prostate respectively. The location of the femoral heads of hip prostheses in a patient with bilateral hip replacement can be seen in Figure 2.6. It should be noted that the hip prostheses lie directly in the path of the lateral beams normally used to treat the prostate. The result of this is discussed later in this chapter. Also worth noting in Figure 2.6 is the dark band running through the implants in the CT image. What should appear as tissue (gray) appears as air (black). This introduces difficulties in critical structure delineation, and is caused by the metal prostheses. The description of how this occurs will require a brief discussion of the theory of computed tomography, given in 2.7.1.

2.6 Critical Structure Delineation in Treatment Planning

The desired anti-cancer activity of radiation takes place only in those tissues directly irradiated by the primary beams. Definition of the tumour, adjacent organs at risk, and other tissues is therefore an essential part of treatment planning to make sure that dose is delivered to cancerous tissues and healthy tissue is spared [9]. All evaluations of the suitability of a treatment plan generated in the planning process implicitly assume that the tumour and organs at risk have been delineated correctly. If they are not, proper evaluation of any plan generated will be flawed, seriously undermining the effectiveness of the planning process.

The cancerous tissue itself can be a well defined tumour, separate from other tissues, or

can be an ill-defined region diffusely located within another tissue or organ. It is up to

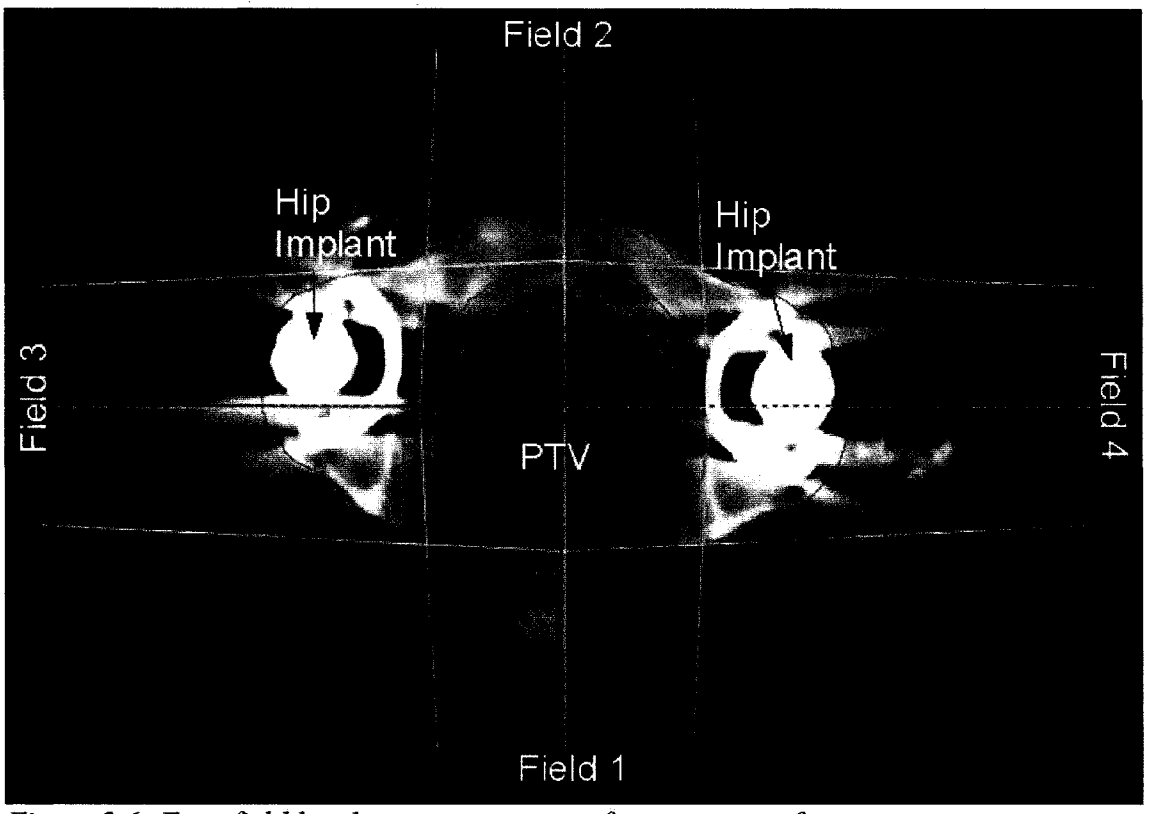

Figure 2.6: Four field box beam arrangement for treatment of prostate cancer.

the oncologist to decide which regions are cancerous and which are not, based primarily on CT images but possibly from a number of different imaging modalities. Since the tumour can be difficult to discern, images should be as information rich as possible.

The International Commission on Radiation Units and Measurements (ICRU) came up with set of standardized definitions which are used today to standardize the various volumes requiring delineation in a radiotherapy plan [10]. They are the gross tumour volume (GTV), the clinical target volume (CTV), the planning target volume (PTV) and the organs at risk (OAR). These can be seen in Figure 2.7. The GTV is "the gross palpable, visible and demonstrable extent and location of the malignant growth" [9]. The CTV is the volume which encompasses all diseased tissue, including microscopic

disease not discernible through examination or imaging. It is generally obtained by adding a somewhat empirical margin concentrically to the GTV. The PTV is the volume that is to be treated day to day to some prescribed dose, and is obtained by adding a margin to the CTV. The purpose of this margin is to account for both organ motion and setup errors which tend to move the CTV around from fraction to fraction. Adding the margin helps ensure that the entire CTV is treated to some minimum dose at each fraction. Also shown in Figure 2.7 are the treated volume (TV) and the irradiated volume (IV). The TV is the volume of tissue that receives the full treatment dose capable of achieving the goal of treatment (eg 95% of the prescribed dose). If dose could be delivered with perfect accuracy, the TV would be identical to the PTV. The IV is the volume of tissue that receives a dose that is significant in comparison to normal tissue tolerance levels.

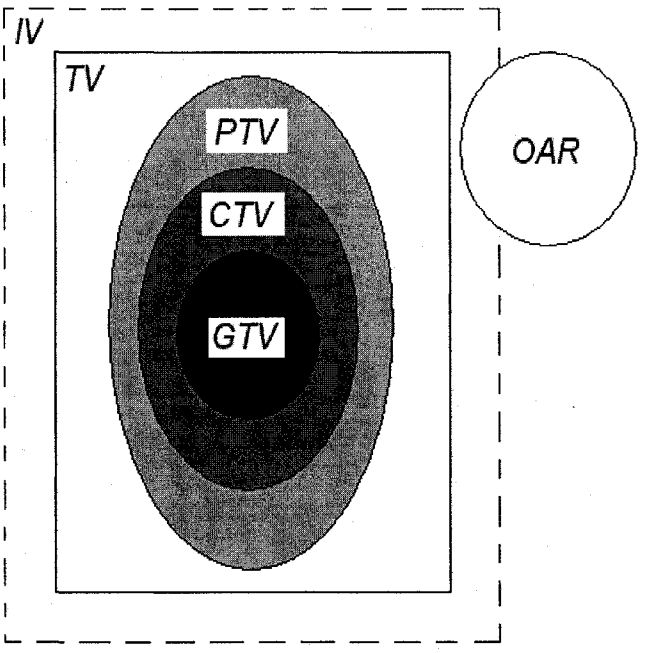

Figure 2.7: The various volumes outlined in ICRU 50 requiring delineation.

2.7 Computed Tomography

2.7.1 General Properties

Computed tomography (CT) is the most widely used imaging modality in radiation therapy. Tomography can be defined as "the cross-sectional imaging of an object from either transmission or reflection data collected by illuminating the object from many different directions" [1]. CT scanners detect x-rays which are directed upon and transmitted through an object in order to come up with a three dimensional reconstruction of that object. Voxels, the three dimensional equivalent of two dimensional picture elements, or pixels, are assigned values according to the average linear x-ray attenuation coefficient, μ, found in the volume they represent. The higher the attenuation in a given volume, the brighter the voxel associated with it. The unit used to describe a voxel based on its attenuation coefficient is called the Hounsfield unit (HU) after Nobel Prize winner Godfrey Hounsfield, the developer of the first clinical CT scanner. Mathematically it is defined as in (2.1):

$$CT_{number}(HU)=\frac{\mu-\mu(w)}{\mu(w)}\times 1000 \qquad (2.1)$$

Where μ represents the average linear attenuation coefficient, measured in the volume represented by a particular voxel, and μ(w) represents the linear attenuation coefficient of water. The linear attenuation coefficient is the constant of proportionality which relates the number of photons (n) remaining in a beam after traversing a medium of thickness (x), and is defined in the following:

$$n=N_0 e^{-mux} \qquad (2.2)$$

where N_0 represents the original number of photons in the beam. The linear attenuation coefficient is in fact the sum of the attenuation coefficients associated with the various interactions a photon can undergo with a material, such as the photoelectric effect,

Compton scattering and pair production. As a result, the linear attenuation coefficient has a complicated dependence on the energy of the photon and the atomic number and electron density of the material through which the photon is propagating. For the energy range and materials encountered in the clinic (1 – 20 MeV and normal body tissues) the Compton scattering interaction dominates, though other interaction mechanisms such as pair production, the photoelectric effect, and to a lesser extent coherent scattering are also possible.

Typical diagnostic CT numbers of selected substances and tissues can be found in Table 2.1.

Tissue or Substance	Typical CT Number
Air	-1000
Bone	232
Solid Water	8
Inner Bone	226
Lung	-529
Brain	30
Cortical Bone	1210
Adipose	-87

Table 2.1: Typical CT numbers for selected substances and tissues

CT numbers have traditionally been 12 bit numbers, allowing for 4096 possible values, usually between -1000 and 3095. This is adequate for tissues normally found within the body, but for denser materials such as the metals used in prostheses a larger range of values is required. Some newer CT systems support 16 bit values, allowing for 65536 possible values, with a CT number range of -1000 to 64535.

Since the invention of the CT scanner in 1972, there have been five technologically distinct variations of CT scanner hardware and software developed. The variations are referred to as "generations" and it is the third generation of scanner that is now clinically the most widely used and therefore the one which will be described in greater detail in

this thesis.

A third generation CT scanner consists primarily of a radiation source and detector system housed in a gantry. The source and detector rotate around a fixed focus point and acquire projection data at multiple angles. The system also has a couch capable of translating objects through the gantry at a constant, controllable speed. To these hardware components is attached a computer capable of processing the basic information acquired by the detector system and coming up with contiguous two dimensional attenuation maps of the object, yielding a three dimensional map.

2.7.2 Filtered Backprojection Reconstruction

2.7.2.1 FBP and Normal Tissue

In order to understand how images are reconstructed in CT, we may consider first generation geometry for ease of understanding without loss of generality, following the lead of Judy [11]. First generation design is pictured in Figure 2.8.

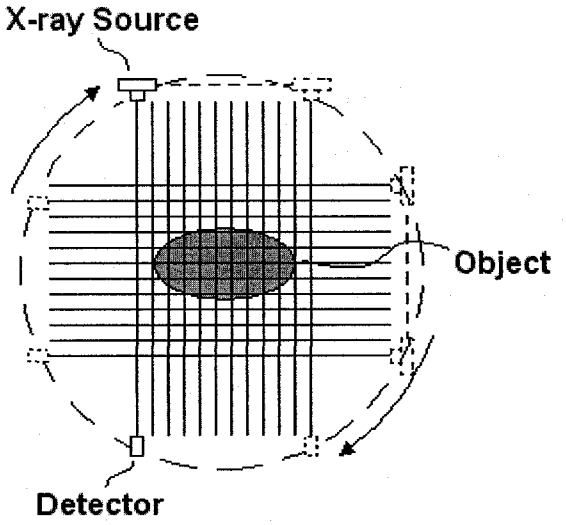

Figure 2.8: First generation CT scanner design. Scanning of the object entails the translation of the source and detector across the field of view, followed by a rotation of the detector and source through some angle. The whole process is repeated to obtain as many projections of a slice as is required.

The coordinate system used to describe this geometry can be seen in Figure 2.9, where the coordinate system (x,y) denotes a stationary reference frame and (x_r,y_r) denotes a frame rotated by the angle φ with respect to (x,y). The directed line (l) in this diagram is one of the possible rays from source to detector pictured in Figure 2.8. Both systems have their origin at the isocenter of the CT gantry. In first generation geometry then, the intensity measured at a given angle φ at some detector located at a given x_r will be:

$$I_\phi(x_r)=I_0 e^{-\int \mu(x_r,y_r)dy_r} \qquad (2.3)$$

Where I_0 is the intensity of the incident beam and $\mu(x_r, y_r)$ is the linear attenuation map of the object in real space, as pictured in the second part of Figure 2.9. It should be noted that this only strictly holds true for a monoenergetic beam, in which case there is in fact a single value for $\mu(x_r, y_r)$ that can be defined. This can be linearized to obtain the following:

$$\lambda_\phi(x_r)=-\ln\frac{I_\phi(x_r)}{I_0}=\int \mu(x_r,y_r)dy_r \qquad (2.4)$$

$\lambda_\varphi(x_r)$ is called the Radon transform of the object distribution. We now have a system of linear equations from which we may find the linear attenuation distribution $\mu(x,y)$ itself from the measurements $\lambda_\varphi(x_r)$. It should be noted that I_0 can be obtained in previous calibration measurements. This system can be solved iteratively or more analytically, but due to computational constraints the iterative approach is of limited practical use. Numerical approximations to the analytic solution, the inverse Radon transform, are therefore used to solve the system. Filtered backprojection is such an approach.

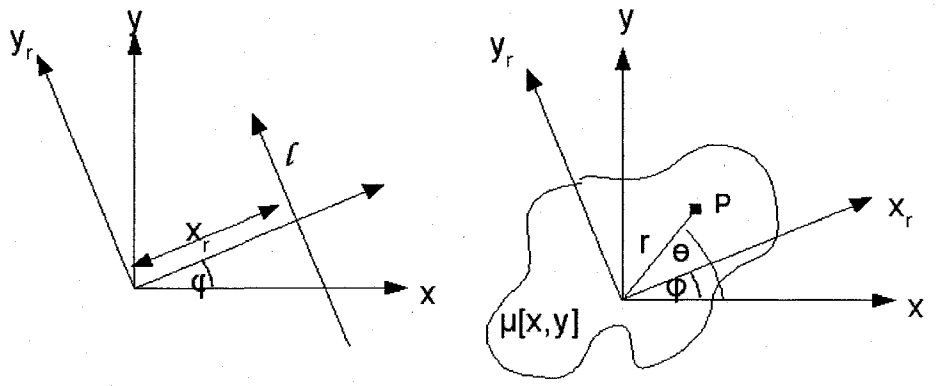

Figure 2.9: Illustration of the coordinate system used in the discussion of filtered backprojection.

Backprojection is a mathematical process wherein one dimensional projection data at a given angle φ is smeared backwards uniformly across the two dimensional object space. That is the value λ_φ for each x_r is added to all y_r for that particular x_r. This is done for all angles φ, and the resultant image is called the summation image. Projection, followed by backprojection, is a linear, shift-invariant process and a point spread function (PSF) can be defined for the procedure. The PSF for this process has a 1/r dependence, thus creating a badly blurred image requiring a filter.

The filtering process is designed to minimize the blurring of the projection – backprojection process by eliminating the 1/r dependence of the PSF for this process. Theoretically one could produce an ideal image using a properly selected filter, though in practice this would only serve to amplify noise at higher frequencies. A function which limits the amplification of higher frequencies, known as an apodizing function, is added to the filter to prevent this. The PSF of this filtered backprojection process is given by the apodizing filter. The filtering can be done either on the one dimensional projection data before backprojection or on the two dimensional summation image after backprojection. The methods are equivalent. Due to time considerations, filtering is carried out on the one dimensional projection data as it is acquired to speed up image reconstruction [12].

2.7.2.2 FBP and Higher Density Materials

As mentioned previously, the filtered backprojection method is only strictly applicable to monoenergetic beams that are scatter free. This is the theoretical setup in which linearity is attained. Any deviation from this setup will introduce non-linearities and will degrade any image reconstructed with this method. There are well known sources of non-linearity in CT images such as scatter, undersampling, and the partial volume effect. Of special importance in the case of a higher density material in the object are beam hardening and photon starvation. Beam hardening arises because the beam is not monoenergetic, and therefore there is no single attenuation coefficient that can be defined in equations (2.3) and (2.4). As the beam travels through an object, lower energy photons are preferentially attenuated, raising the average energy of the beam and making it more penetrating. Voxels located toward the center of an object will therefore appear less dense than they actually are since the portion of the beam that passes through them will always have been hardened in this way. CT manufacturers typically apply a polynomial correction function to the measured attenuation data from the x-ray detectors to approximate the ideal attenuation data for a monoenergetic x-ray beam [13]. This correction is not optimized for metal, and thus becomes a major source of artifacts [13] [14]. Photon starvation arises because the portion of the beam passing through a metal implant is attenuated to the point that very few photons get to the detector. This is what prevents kVCT systems from properly assigning CT numbers to voxels containing metals. The measured signal is dominated by quantum noise [12] and there are gaps in the projection data which are not properly reconstructed with standard algorithms [15]. All of the above will be present in any image of an object containing metal. The cumulative effect can be seen in Figure 2.10 which shows a CT slice of a patient with bilateral hip prostheses.

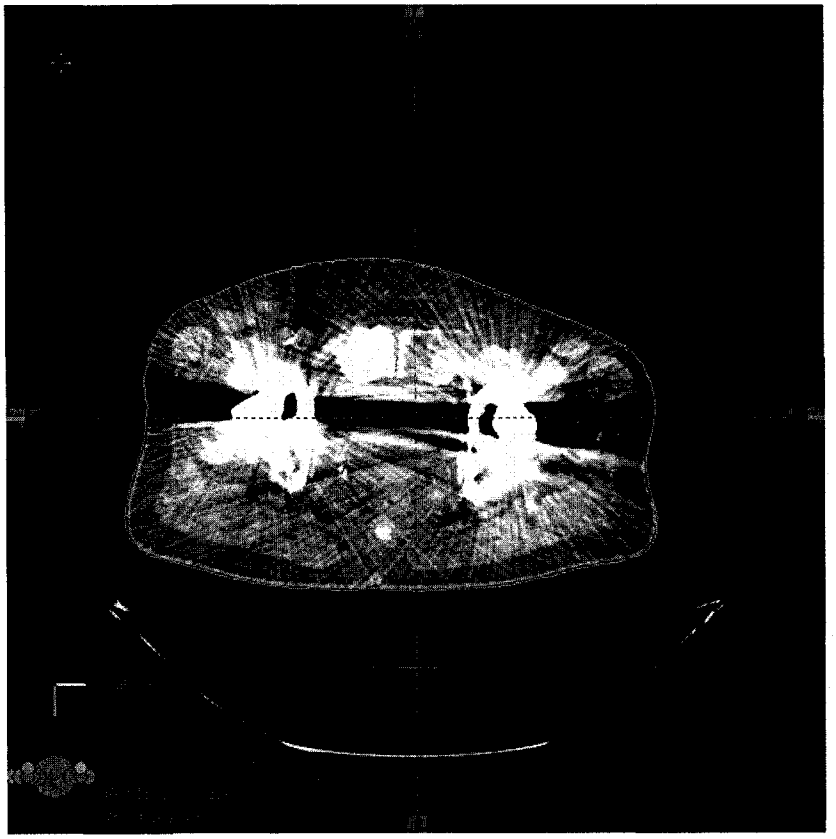

Figure 2.10: Diagnostic CT image of a patient with bilateral hip prostheses demonstrating the detrimental effect of metal in filtered backprojection.

As noted earlier, regions of the image which should appear as gray, signifying soft tissue, appear black, signifying air. The CT numbers in this image are therefore unfit for use for conversion to electron densities for dose calculations. All anatomical information in the region between the hip prostheses, where the prostate, bladder and rectum lie, has also been lost. This presents difficulties for the initial delineation of critical structures. Furthermore, if the image is obtained with a CT system only capable of yielding 12 bit CT values, the CT numbers given for the metal prostheses will be bounded by the maximum 12 bit value of 3095, as CT numbers usually begin at -1000. When this capped value is used in dose calculations, the electron density used by the dose calculation algorithm for the metal will be too low.

2.7.2.2.1 Details Regarding Hip Prostheses

As the population ages, prosthetic devices including hip prostheses will become more common and therefore so will the frequency of problems associated with planning treatments for these patients [16]. The American Association of Physicists in Medicine Task Group 63 found in a survey of 30 institutions that between 1% - 4% of patients had prosthetics which could affect their treatment [16]. Prosthetic devices made of high Z materials such as steel can be found in numerous forms in the body, including: mandibular plates for reconstruction, hip, leg, and arm prostheses, spinal cord fixation devices, surgical rods, stents, and various dental fillings [16].

There are numerous types of hip prostheses that are currently in use. The various parts of a typical prosthesis used in a total hip replacement can be seen in Figure 2.11 [17]. The three separate pieces are: the acetabular cup, the femoral head and the femoral stem. The assembled femoral stem and head can be seen in Figure 2.12 [17]. The acetabular cup consists of a polyethylene core supported by a Co-Cr-Mo or Titanium shell. The femoral stem and head are most often constructed of Titanium or Co-Cr-Mo, but stainless steel has also been used and is still encountered in the clinic. The femoral heads and stems can be either hollow or solid [16].

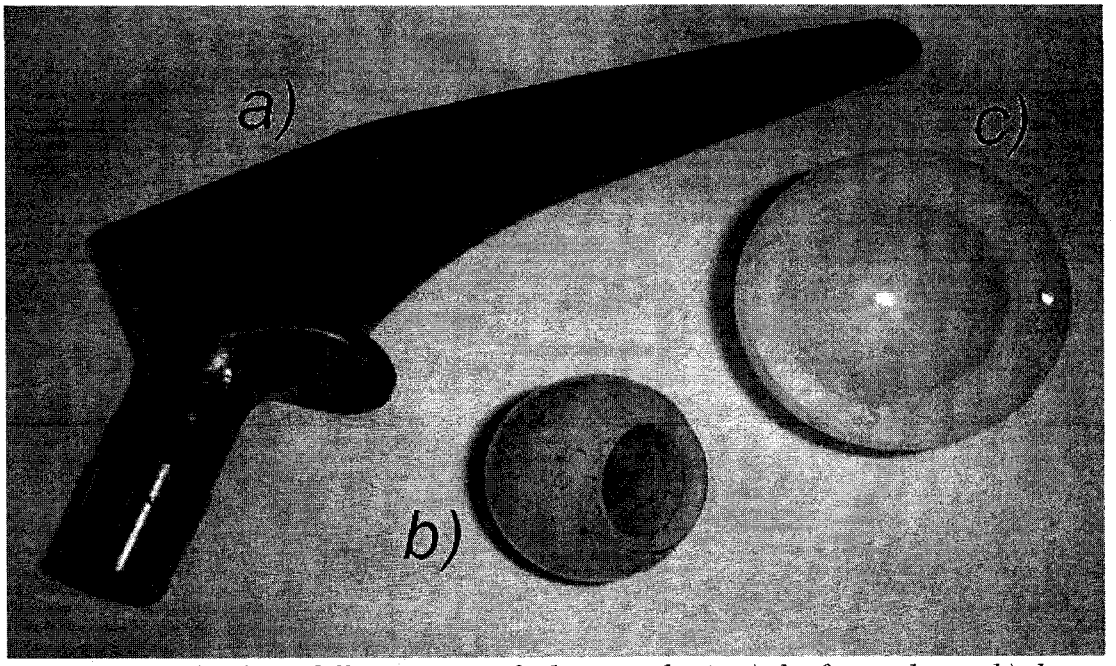

Figure 2.11: The three different parts of a hip prosthesis a) the femoral stem b) the ball and c) the acetabular cup.

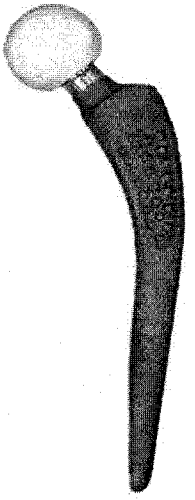

Figure 2.12: The assembled femoral stem and head.

The characteristics of the three metals used in hip replacement can be found in Table 2.2

and Table 2.3 [16]. The electron density is the number of electrons per unit volume of a material. In radiotherapy, this value is often given relative to water. The value listed for Co-Cr-Mo (6.74) for instance means that Co-Cr-Mo has 6.74 times as many electrons per unit volume as does water. The physical density, also known as the mass density, is simply the ratio of the mass of a substance to its volume.

Material	Electron Density Relative to Water	Physical Density (g/cm^3)	Effective Atomic No.
Co-Cr-Mo	6.74	7.9	27.6
Titanium	3.6	4.3	21.4
Stainless Steel	6.83	8.1	26.7

Table 2.2: Physical properties of metals used in hip prostheses.

The important characteristics of an implant from a dosimetric point of view are the size, the shape, the type of metal used and the hollowness of the implant. These must be known before accurate dose calculations can be carried out.

Element	Stainless Steel	Co-Cr-Mo	Titanium
Carbon	0.08 max	0.35 max	0.08 max
Manganese	2.00 max	1.00 max	X
Phosphorus	0.03 max	X	X
Sulfur	0.03 max	X	X
Silicon	0.75 max	1.00 max	X
Oxygen	X	X	0.13 max
Cobalt	X	Balance (57.4 – 65)	X
Chromium	17 – 20	27 – 30	X
Nickel	10 – 14	2.50 max	X
Molybdenum	2 – 4	5 – 7	X
Iron	Balance (59 – 70)	0.75 max	0.25 max
Aluminum	X	X	5.6 – 6.5
Vanadium	X	X	3.5 – 4.5
Titanium	X	X	Balance (88.5 – 91)

Table 2.3: Elemental composition of the three metals used in hip prostheses (stainless steel, Co-Cr-Mo, Titanium). Numbers are in percent. X signifies that an element is not present in the implant metal.

2.7.3 Methods of Dealing With Metal Artifacts

Since the corruption of the CT data affects both the anatomical and electron density information available, it is important that metal artifacts are dealt with. The reduction of metal artifacts to recover anatomical information in the images is a relatively new and growing area. Several algorithms [13][14][15][18][19][20][16] for the reduction of artifacts have been proposed, but until recently there were none commercially available. Exactly how these algorithms work is beyond the scope of this thesis, but they are capable of greatly reducing metal streak artifacts in CT images. This recovers much of the anatomical information of structures in close proximity to the implant. They are unable, however, to provide suitable CT numbers for the prosthesis itself. This is due to the fact that diagnostic energy photons are largely unable to penetrate metal, and therefore any value obtained for μ in equation (2.1) with these photons will be inaccurate due to a very low signal-to-noise ratio.

Despite the fact that these algorithms have been developed, there are still a number of centres which do not have artifact reduction capabilities at present, including ours. This is because the bulk of these algorithms have been developed in-house and are therefore not commercially available.

The American Association of Physicists in Medicine (AAPM) Task Group 63 reports that in a survey of 30 institutions, there was no general consensus regarding proper treatment for patients with hip prostheses, despite the fact that between 1%-4% of patients had prosthetics which could affect their treatment [16]. There are several practices being implemented to help overcome this problem. Institutions may:

1. Ignore the presence of the device altogether.
2. Use beam arrangements which avoid implants as much as possible to minimize errors in dose calculations caused by inaccurate electron density information of the implant. Artifacts are either ignored or inhomogeneitry corrections are not used, to prevent the use of incorrect CT numbers. These arrangements often lead to escalated doses in critical structures adjacent to the planning volume.

3. Treat through an implant provided the doses are low enough that the presence of metal does not create any extra complications.
4. Take into account the metal prostheses in the planning process using hand calculations or treatment planning software if the characteristics of the implant are known (density, thickness, etc.).
5. Use compensators to boost the dose in the shadow of the metal implant so that the dose distribution behind the implant is uniform.

For treatment planning, the task group recommends finding out all limitations to treatment planning software and dose calculation algorithms. Beam arrangements which avoid the prosthesis should be considered first. If this is possible, the patient may be planned as usual either with metal streak artifacts edited out or with no tissue inhomogeneity correction. If avoiding the prosthesis is not possible then the process is more complicated and the details depend on whether or not data on the prosthesis is available. If data on the prosthesis is available, physical characteristics such as dimensions and electron density should be gathered for use in treatment planning. Dimensions may be obtained from orthogonal simulator films for example. Treatment planning may then proceed with the proper electron density for the prosthesis manually entered into the treatment planning system. Published data on prosthesis attenuation and electron densities may be used for comparison purposes. During simulation, portal images should be taken to confirm if the prothesis is hollow or solid if this information is not in the patient's record, and exit dose measurements taken to confirm the calculated attenuation of the prosthesis [16].

If there are no data available, treatment planning should be carried out first, with no heterogeneity corrections. If possible, on the first day only films should be taken. If not, the first fraction should be given ignoring the presence of the prosthesis. During this fraction, films or an EPID should be used to check to see if the device is hollow or solid. Exit dose measurements should also be taken with films or thermoluminescent dosimeters. From these measurements, physical properties of the device can be derived, possibly allowing identification of the type of prosthesis. Treatment planning may then

be carried out again, this time with heterogeneity corrections and the measured data entered into the treatment planning system. In the next fraction, exit dose measurements should be performed to confirm the calculations [16].

However treatment planning is accomplished for patients with hip prostheses, it clearly involves more work than for patients without prostheses due to the fact that delineation of the critical structures can be more difficult and calculation of dose distributions is not as reliable and therefore requires more consideration. Much of this stems from the inability of kVCT photons, chosen for optimal imaging of normal tissues, to adequately image patients with metal prostheses.

2.7.4 Megavoltage Computed Tomography

One of the future developments listed in the TG-63 report which "may help produce streak-free images" [16] is megavoltage computed tomography (MVCT). MVCT is computed tomography using a megavoltage beam. This is essentially the only difference, though slight modifications, for example in detector systems, are made to adjust to the higher energy. MVCT units have utilized cobalt as the source of photons [21], but the more common source of MV photons is the linear accelerator (e.g. TomoTherapy Inc. [22]).

A linear accelerator is a device capable of producing photon beams with a greater peak energy than can be produced in a x-ray tube. The electrons used to produce the Bremsstrahlung photons are accelerated not by a potential difference, as in x-ray tubes, but by a waveguide. A waveguide is a device which uses microwave frequency electromagnetic energy (~3000 MHz) to set up a standing wave pattern in a series of cavities. Electrons are injected into and travel down the waveguide in such a way that they only pass through cavities with an electric field of one direction or zero. This arrangement can easily produce beams of 25 – 35 MeV. These electrons then impinge upon a target, resulting in the release of Bremsstrahlung photons, directed mostly in the forward direction.

The main anticipated advantage of using MVCT over kVCT for imaging patients with

metal prostheses comes from the greater energy of the beam. The greater energy of the beam increases its penetrability and decreases the amount of photon starvation experienced at the detector. This greatly reduces one source of metal artifacts. Since the MVCT photons will penetrate metal more effectively than kVCT photons, it may be possible to accurately measure μ in equation (2.2) and obtain proper CT numbers for the prostheses. This eliminates the need to manually enter in CT numbers or electron densities for metal. The MVCT beam also does not suffer from beam hardening to the extent that a kVCT beam does, since the total attenuation coefficient at MV energies is less sensitive to changes in energy than at kV energies. This makes the assumption of linearity used in reconstruction discussed in 2.7.2.1 less egregious for MV beams than for kV beams. It also makes MVCT number-to-electron density calibration of the images easier, since the CT number assigned to any given material will not have as strong a dependence on the depth of the material inside the phantom [23].

The strength of MVCT is also its weakness. The lower energy of diagnostic CT units is chosen because it maximizes the contrast between normal tissues of interest in the body, especially softer tissues. The ability of CT to distinguish soft tissues is marginal even with this lower energy choice when compared to a modality such as magnetic resonance imaging (MRI). What was difficult to distinguish with diagnostic imaging (prostates for example) becomes even harder with the loss of soft tissue contrast accompanying the increase in energy. The higher average energy of the MV photons also implies more dose deposited per photon compared to kV photons, and so fewer photons must be used to keep the doses comparable. This increases the noise in MVCT images [24]. The photons are also harder to detect given that they are more penetrating, but this is mitigated by the fact that more of them make it to the detector in the first place.

If the use of MVCT offers the advantages listed above, the planning process for patients with hip prostheses will be greatly simplified and improved. Images will not suffer as badly from metal artifacts, which is important for delineating critical structures, and little or no extra attention will need to be given to dose calculations. Treatment planning may proceed as usual, with MVCT images used for treatment planning and dose

calculations instead of kVCT images. This improvement and simplification of treatment planning for patients with prostheses requires a dose calculation algorithm capable of accurate calculations in the presence of metal.

2.8 Treatment Planning Systems

A treatment planning system (TPS) is the hardware and software that bring together the dose calculation algorithm and numerous other tools such as DICOM import/export, CT volume definition, DICOM image registration, radiation field placement, dose volume histograms, dose distribution addition, as well as a host of other functions necessary to plan and deliver treatments in a clinical setting. A complete description of treatment planning systems is beyond the scope of this work.

Treatment planning software allows for patient data in the form of diagnostic images (CT, MRI, PET, etc.) to be imported and used by the dose calculation algorithm in order to calculate dose distributions on a particular patient. Treatment planning systems will contain tools which can be used for the manipulation of diagnostic images so that all of the information required can be obtained. This includes window and leveling tools, contouring tools for delineating structures of interest, area and volume measurement tools and others. The exact tools included in different treatment planning systems will vary. Likewise, the dose calculation algorithm included in different systems will differ from vendor to vendor, as well as over time.

2.8.1 Dose Calculation Algorithms

2.8.1.1 Commercially Available Algorithms

A dose calculation algorithm is a program in the treatment planning system used to calculate dose distributions in a phantom or patient resulting from the application of a given beam arrangement, using CT images of the phantom or patient. This is accomplished through the conversion of CT images to electron density maps, using a suitable CT number – to – electron density ramp, measured beforehand. Though there

are several methods by which radiation may interact with matter, at the energies used in radiotherapy the Compton or incoherent scattering process dominates. The cross section of the next most probable interaction for carbon for example ranges between 0.06% and 5.3% that of the Compton scattering cross section for photon energies ranging between 1 and 4 MeV [25]. For a photon of a given energy, the total cross section for Compton scattering, known as the Klein-Nishina cross section, is a constant. Estimation of the dose absorbed by a material to within a few percent, in most cases, therefore only requires knowledge of the electron density of the material. No commercial dose calculation algorithm takes into account any other photon interaction (pair production, coherent scattering, photoelectric effect, etc.).

There are two broad categories of dose calculation algorithms that have been used or are in use clinically. The earliest and simplest of these was the broad-beam or empirical algorithm, which makes use of tabulations of beam data in simple geometries such as in water phantoms to estimate the dose distribution resulting from the application of that beam to a more complex geometry. Despite the fact that the quantities used to calculate dose distributions are defined for very simple geometries, "they give reasonable results in the vast majority of clinical situations" [26]. They become insufficient however when the situation is more complex or when greater accuracy is required, for example when fields are intensity-modulated or when dose-escalation protocols are implemented.

Superposition algorithms belong to the second category of algorithms and are the most widely used in clinical situations today. The basis of the algorithm can be seen in Figure 2.13.

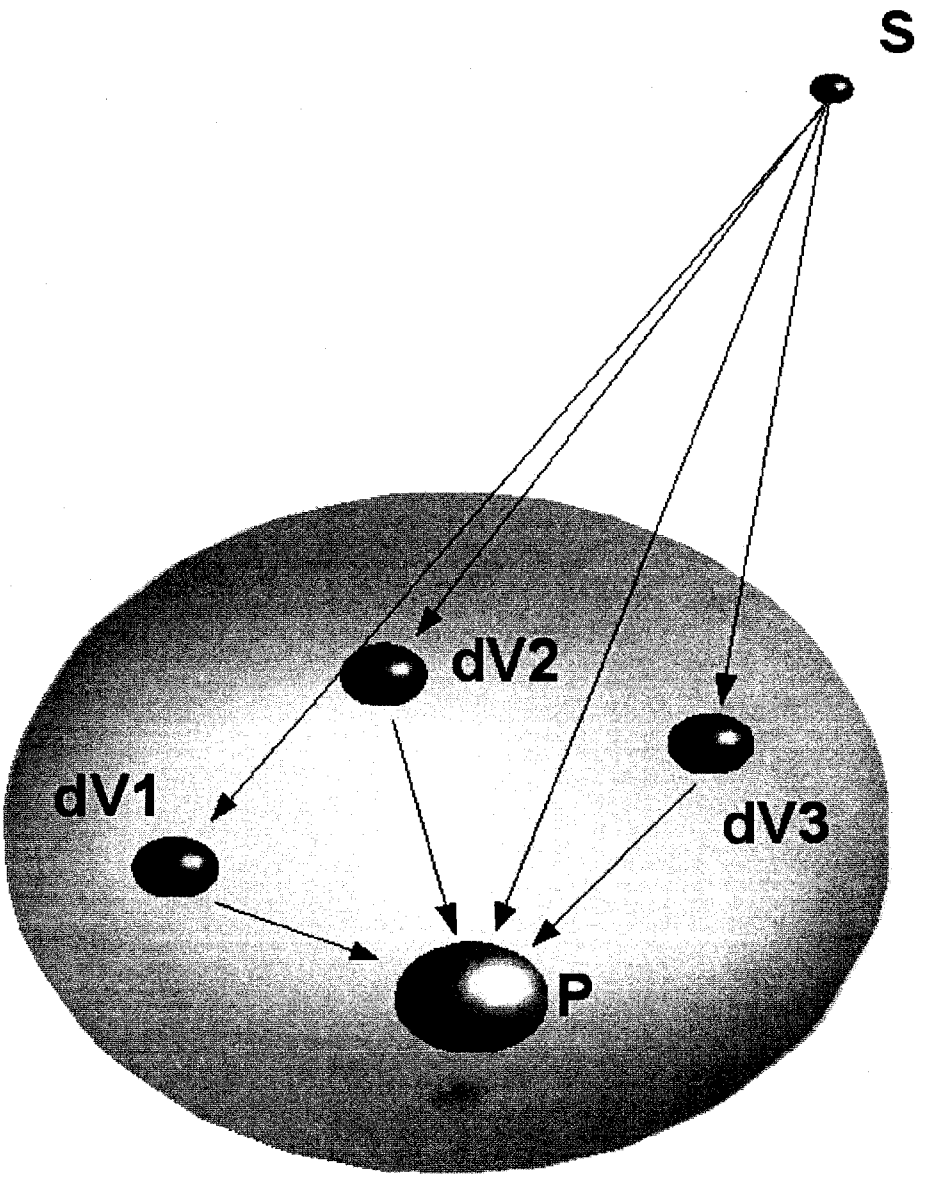

Figure 2.13: The fundamental principle of the superposition method. The dose at point P can be calculated by summing the primary energy contributions at P with the energy contributions to a small volume around P originating from primary interactions in the volume elements dVi. Though only single scatter contributions are shown, contributions to P from multiple scattering events must also be included.

The two superposition algorithms which predominate today are the pencil beam kernel and the point spread kernel. Both are an acceptable compromise between speed and accuracy given the computing power of the present, however the pencil beam algorithm

is faster than the point spread algorithm, while the point spread algorithm handles inhomogeneity correction more accurately. The pencil beam algorithm "suffers inherently from serious limitations in handling inhomogeneity corrections properly since the pencil beam is generally treated as a whole" [26].

Ultimately, all commercial dose calculation algorithms suffer from the same shortcoming: they are analytic fit solutions based on dose deposition in water, and do not easily take inhomogeneities into account, though some are better than others. The most advanced of these, the 3D convolution of point spread functions, uses kernels derived from simulation in water, and the kernels are approximately scaled to accomodate non-water materials found in a patient. In cases where materials are present which have densities vastly different from water, the dose distributions calculated with commercial dose calculation algorithms may be unsatisfactory. Commercial dose calculation algorithms therefore need to be checked against more accurate calculations or measurements. The Monte Carlo algorithm offers one method of checking accuracy.

2.8.1.2 The Monte Carlo Algorithm

The Monte Carlo dose calculation algorithm tracks individual particles, keeping track of interactions they undergo, dose they deposit and subsequent particles they produce. The Monte Carlo method therefore has the ability to calculate dose distributions to arbitrary precision, only limited by the number of particles simulated. This is possible because the interactions that individual particles undergo as they traverse a medium are well understood and can be simulated with a high degree of accuracy. The downside to Monte Carlo and the reason it has not supplanted analytic fit algorithms clinically is because it is presently computationally expensive and cannot achieve the speed of analytic fit algorithms. Furthermore, in sites of the body which are largely homogeneous, the improved accuracy of Monte Carlo is not required since analytic fit algorithms already achieve the required accuracy.

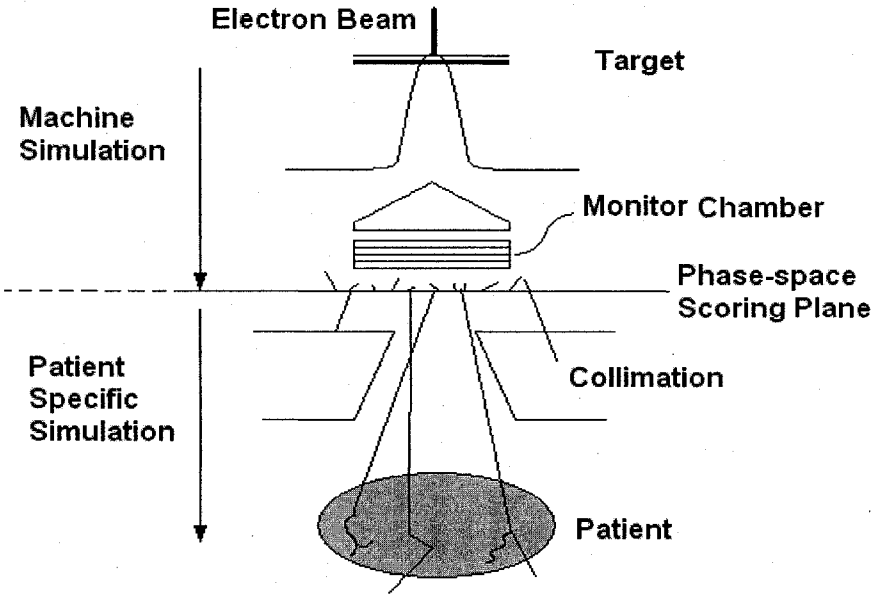

Figure 2.14: The two steps involved in dose calculations using the Monte Carlo algorithm.

The Monte Carlo algorithm can be split up into two phases. The first deduces the characteristics of the particles to be used in the simulation such as type (e.g. photon, electron, positron), energy and direction. This data set is referred to as the phase-space and is computed first. The second is the calculation of the dose to the patient, using the particles contained in the phase-space. The two steps can be seen in Figure 2.14.

The phase-space can be obtained using the Monte Carlo code itself, simulating the electron beam of the linear accelerator from the point that it leaves the vacuum window before it impinges upon the target. An alternative method that requires less storage space uses multiple virtual radiation sources to model the various sources of radiation such as the target, and sources of scatter such as the primary collimator and the flattening filter. These virtual sources sum to model the beam for a given treatment head design. The phase-space is reconstructed from the virtual sources when needed [27].

Once the phase-space has been obtained, calculation of the dose delivered to a patient or phantom can be completed. This is done by transporting particles in the phase-space to the phantom, and using fundamental physical principles to decide when and where they interact with the medium, through what mechanism, how much energy is deposited and

what particles are created in turn. All of this is done with the help of a random number generator which will make the entire process stochastic, but with values chosen weighted by the known cross-sections or probability distributions so that values such as mean path length, number of Compton interactions and dose will tend towards their expectation values after enough histories have been run. Referring to Figure 2.15, we can get a better sense of how this is done for photons.

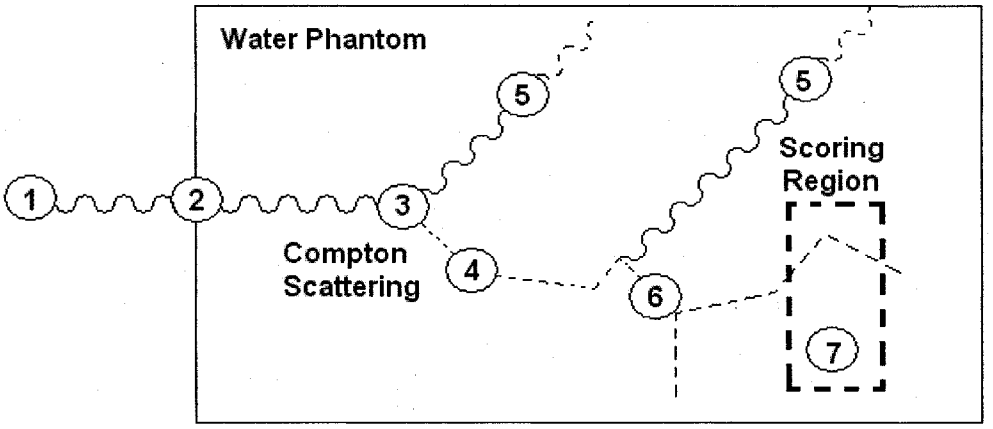

Figure 2.15: A single history in a Monte Carlo dose calculation.

A photon at (1) is transported to the medium (2) to be irradiated, in this case a water phantom. At this point, the computer will decide the distance it will travel and will transport the photon this distance (3). At (3) the computer will decide which type of interaction the photon will undergo (Compton, photo-electric, pair-production, etc.) at random, but based on the cross-sections for such events for the energy of the photon and material in question. In this example, it is a Compton scattering event. The scattered photon is then set off on a new direction, and travels to (5) where we no longer concern ourselves with it as it has either exited the phantom, or its energy has fallen below some threshold value and we assume complete local dose deposition. The compton electron generated at (3) is then transported along its path (dotted line) and all δ-rays and bremsstrahlung photons produced along the way are tracked (6). Finally, the deposited energy, fluence spectra and other quantities of interest are scored in some region of interest (7) [28].

For electrons, the calculation has to be sped up due to the fact that each relativistic

electron will undergo 10^5 to 10^6 interactions before slowing down. For comparison, each photon undergoes only a few before exiting the phantom, which allows for every interaction to be modeled in its entirety. Fortunately, there are simplifications that can be used which do not overly sacrifice accuracy. Though electrons interact more often than photons in their transport, few of these interactions cause significant change in direction or loss of energy. These can then be combined into fewer large events. Energy loss can be calculated using the continuous slowing down approximation (CSDA) so that the energy loss can be calculated using the stopping power [28]. Different versions of the Monte Carlo algorithm, though identical in their accounting of photon interactions, will differ in how they deal with electron transport.

2.9 Dose Measurement

The second method by which dose calculations can be verified is by comparison to measurements. Detailed dose measurements are not always possible in complex phantoms or patients, but are the preferred method in simple cases such as in water or solid water phantoms.

With both the Monte Carlo method and direct measurement at our disposal, it will be possible to assess the accuracy of a clinical dose calculation algorithm in calculating dose distributions in the presence of a metal prosthesis. If our clinical dose calculation algorithm is capable of calculating doses accurately, and if the other assumptions about the advantages of using MVCT images for treatment planning for patients with hip prostheses hold true, we will have found a formidable tool for use in treatment planning when prostheses are present.

Chapter 3: MVCT Number to Electron Density Calibration

3.1 Objective

The objective of this chapter is:

1. To confirm that the CT number-to-electron density calibration curve measured for the TomoTherapy HI·ART II treatment delivery unit in MVCT imaging mode is independent of phantom positioning and plug arrangement and to measure it so that MVCT images acquired with the unit may be used for treatment planning purposes.
2. To verify that MVCT images are less adversely affected by the presence of metal than diagnostic CT images.

Previous work has demonstrated that the CT number-to-electron density calibration curve for MVCT images generated by the imaging mode of the TomoTherapy HI·ART II unit is independent of phantom and plug arrangement and can be easily measured [29][23] and used in treatment planning calculations with accuracy similar to kVCT images [23]. In this chapter we verify this and measure the calibration curve for our unit by imaging a solid water phantom with tissue equivalent and metal plugs in different arrangements with the TomoTherapy unit. These images are also used to assess the impact of metal artifacts on kVCT and MVCT images.

3.2 Methods and Materials

3.2.1 Materials

The list of materials used in this portion of experiments can be seen in Table 3.1. A short description of each piece follows.

Item	Description	Manufacturer
IMRT plan cheese phantom and plugs	Solid water phantom and exchangeable plugs	Gammex rmi, Middleton, WI, USA
ImageJ 1.34s	Dicom viewer with basic analysis tools	Wayne Rasband, National Institute of Health, USA
TomoTherapy HI·ART II system	Treatment delivery system with MVCT imaging mode	TomoTherapy Inc., Madison, WI, USA
Picker PQ5000 CT unit	A 16-bit kVCT diagnostic CT scanner	Picker International Inc./Philips Medical Systems, Andover, MA.

Table 3.1: List of Materials used for MVCT number-to-electron density calibration of the Helical TomoTherapy Unit.

3.2.1.1 TomoTherapy HI·ART II Treatment Delivery System

The system we have used in this work is the TomoTherapy HI·ART II treatment delivery system (TomoTherapy Inc., Madison, WI) shown in Figure 3.1. It is primarily designed for treatment delivery through the use of a conventional 6 MV linear accelerator and detector system mounted in a CT-like gantry, and is able to deliver dose in a continuous helical fashion in the same way that diagnostic CT units deliver dose for the purpose of acquiring images. A 64 leaf binary multileaf collimator (MLC) is used to modulate the intensity of the beam during treatment delivery. Each leaf is 6.25 mm wide, and can be placed in one of two positions: in or out of the field (hence the term "binary"). The HI·ART II system has an imaging mode in which MVCT images can be acquired. In this mode, the linear accelerator generates a 3.5 MV beam and the fan beam is collimated to a size of 5 mm by 400 mm. It has three acquisition modes (fine, normal and coarse) which control the pitch ratios, or ratio of 1, 1.6 and 2.4 respectively [23]. The pitch ratio is defined as the table increment per 360° of rotation divided by the nominal scan width. The images are reconstructed on an image matrix of 512 × 512, and the field of view has a diameter of 386 mm. The detector system used in the HI·ART II system is a GE 9800 Xenon gas ionization detector system. The system

employs arrays of chambers containing xenon pressurized at roughly 5 atm. Septa are used to separate the chambers and are kept at high voltage differences so that charged particles in the gas, liberated upon interaction with x-rays, are collected in the septa. There are 736 such chambers in the detector.

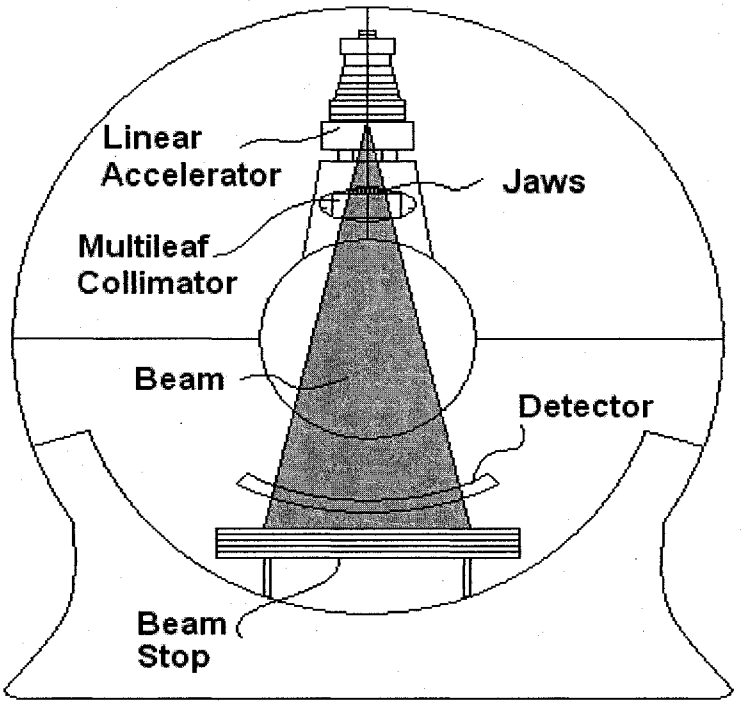

*Figure 3.1: A schematic diagram of the TomoTherapy HI*ART II treatment delivery system.*

3.2.1.2 Picker PQ5000 CT Unit

The CT unit used for comparison purposes in this work is a Picker PQ5000 CT unit (Picker International Inc./Philips Medical Systems, Andover, MA).

3.2.1.3 IMRT Plan Solid Water Phantom

This phantom can be seen in Figure 3.2. It consists of a solid water cylinder with a diameter of 30 cm and 20 larger cylindrical holes which may house cylinders of solid water or different tissue equivalent materials, called plugs, and smaller holes which may hold ion chambers or solid water plugs.

Various tissue equivalent and metal plugs were used in our experiments. The materials we used are summarized in Table 3.2. The type of steel that was used in the fabrication of the two steel plugs listed was unknown. The electron and mass density listed are averages of the types of steel sold by Goodfellow Corporation (Huntingdon, England), which supplies metals to our machine shop. All of the plugs except the steel, aluminum and lead plugs were made and provided by Gammex rmi (Middleton, WI). The electron and mass densities listed for the plugs were also determined by Gammex.

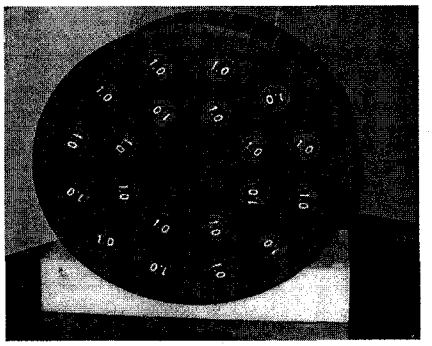

Figure 3.2: The IMRT plan cheese phantom, shown with water equivalent plugs inserted into the 8 inner and 12 outer holes.

Material	Electron Density (Relative to Water)	Mass Density (g/cm^3)
Steel	6.593	7.860
Aluminum	2.334	2.699
Lead	8.098	11.350
Bone (CB2-50% Mineral)	1.47	1.56
Bone (B200)	1.11	1.15
CT Solid Water	0.99	1.02
Breast	0.96	0.99
Inner Bone	1.09	1.12
Lung (LN-450)	0.40	0.45
Lung (LN-300)	0.28	0.30
Liver (LV1)	1.07	1.08
Brain	1.05	1.05
Bone (CB2-30% Mineral)	1.28	1.34
Cortical Bone (SB3)	1.69	1.82
Adipose (AP6)	0.90	0.92
Air	0.00	0.00

Table 3.2:Tissue equivalent and metal plugs used in the MVCT number-to-electron density calibration.

3.2.1.4 ImageJ Dicom Viewer

ImageJ is a program with the ability to view and analyze DICOM images. It allows the user to adjust window and level settings as well as select different regions of interest (ROIs). The ROIs can be any of a number of shapes. Statistics such as the mean pixel value or CT number, its standard deviation and the maximum and minimum values within the ROI can be obtained [30].

3.2.2 Methods

3.2.2.1 MVCT Calibration Scans

The following calibration procedure was adapted from K J Ruchala et al's calibration of their own TomoTherapy MVCT system [29].

The phantom was scanned with two different plug arrangements and with the phantom displaced from isocenter to investigate the dependence of the CT numbers on plug depth and plug location relative to isocentre. Three plug arrangements were used as shown in Figure 3.3. Scans with arrangement (a) and (b) were taken with the metal plugs both present and absent in order to study the impact of the artifacts they introduce on the measured CT numbers of other plugs. The holes were left empty (i.e. filled with air) when the scans were taken with metal absent. All plugs except aluminum were scanned at two different phantom depths. This was done to see if the measured CT number changed due to the hardening of the beam as it traveled through the phantom.

Plug Arrangement 1

The phantom was aligned with the room lasers so that the cylindrical phantom was coaxial with the CT bore. The plugs were placed according to Figure 3.3 (a). The phantom was scanned twice, once with the metal plugs present and once with the metal plugs absent. In both scans, 8 CT slices were reconstructed using a slice spacing of 2.5mm.

Plug Arrangement 2

With the phantom aligned coaxially with the CT bore, the plugs were inserted as shown below in Figure 3.3 (b). 8 CT slices were again reconstructed with a slice spacing of 2.5mm with metal plugs both present and absent.

Plug Arrangement 3

The plugs were arranged as for plug arrangement 1, except the phantom was displaced 5cm laterally from the center of the bore so that the phantom and the bore were no longer coaxial. 8 CT slices were generated with a slice spacing of 2.5mm. This scan was not repeated with the metal plugs absent.

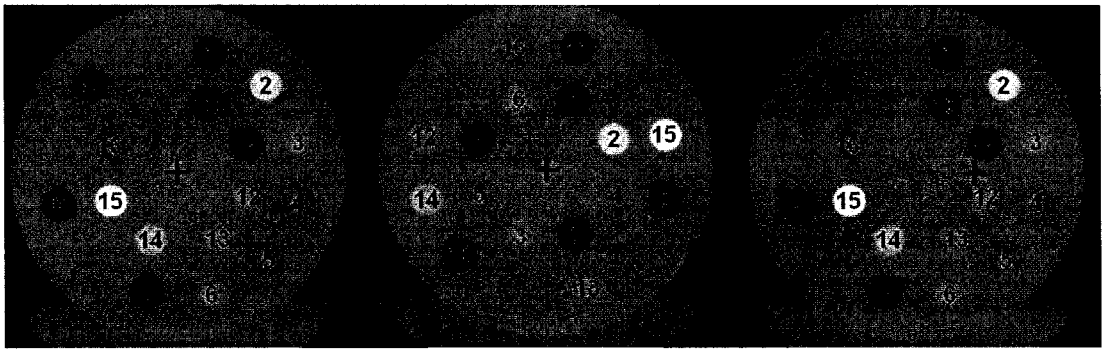

(a) *(b)* *(c)*

1 – Steel *2 – CB2-50%* *3 – B-200* *4 – Solid Water* *5 – Breast*

6 – Inner Bone *7 – Steel* *8 – Lead* *9 – Aluminum* *10 – LN-450*

11 – LN-300 *12 – Liver* *13 – Brain* *14 – CB2-30%* *15 – Cortical Bone*

16 – Adipose

Figure 3.3: The three plug arrangements used in the calibration experiment. Plugs which lay at shallower depths in the first arrangement (a) are placed deeper in the phantom in the second arrangement (b). The red cross denotes the approximate location of the CT isocentre. The plug arrangement in (c) is identical to arrangement (a), with the entire phantom shifted inside the bore.

The resulting images were analyzed using the DICOM image viewer ImageJ. A circular ROI was drawn with a diameter of roughly two-thirds the diameter of the plugs in the images and placed in the center of each plug. An analysis tool in the program measured the mean pixel CT value in the ROI, its standard deviation, and also the maximum and minimum pixel values. These were recorded for three separate slices in each of the studies away from the ends of the plugs to include odd and even slices, and the weighted mean and the average standard deviation were found using the following formulae:

$$\bar{x} = \frac{\sum \frac{x_i}{\sigma_i^2}}{\sum \frac{1}{\sigma_i^2}}, \qquad \sigma = \frac{\sum \sigma_i}{N} \qquad (3.1), (3.2)$$

where x_i is the average pixel value of a given ROI in the different slices, σ_i is the standard deviation of that same ROI in the different slices and N is the number of slices. The resulting average values were plotted against the electron densities of the various tissue equivalent plugs as summarized in Table 3.2.

3.2.2.2 kVCT Calibration Scans

The phantom was scanned in the Picker PQ5000 unit in order to compare the effects of metal artifacts in MVCT and kVCT images. The phantom was aligned with the room lasers so that the cylindrical phantom was coaxial with the CT bore. The plugs were placed according to Figure 3.3 (a). The phantom was scanned twice, once with the metal plugs present and once with the metal plugs absent. The phantom was helically scanned at 130 kVp, a slice thickness of 3mm and an exposure of 8900 mAs.

The images were analyzed using ImageJ as described for the MVCT images.

3.3 Results and Discussion

3.3.1 MVCT Calibration Measurements

The measured values for the mean CT number for each plug, along with its standard deviation for the various scans can be seen in Table 3.3. Plots of the measured mean CT numbers for the plugs versus their electron densitites are shown in Figure 3.4 and Figure 3.5.

Plug-by-plug comparison	Arrangement 1 - Metal		Arrangement 1 - No Metal		Arrangement 2 - Metal		Arrangement 2 - No Metal		Arrangement 3 - Displacement	
	Mean	Std. Dev.	Mean	Std. Dev.	Mean	Std. Dev.	Mean	Std. Dev.	Mean	Std. Dev.
CB2-50%	504	47	487	40	496	73	476	51	485	47
Bone	143	56	144	40	183	76	113	51	147	48
Solid Water	23	45	23	40	15	83	27	48	19	44
Breast	-3	49	-7	42	50	65	-2	45	-9	52
Inner Bone	144	53	125	41	207	77	124	48	130	51
Lung I	-472	85	-496	49	-480	55	-506	42	-488	61
Lung II	-670	66	-665	49	-703	66	-679	36	-646	64
Liver	85	60	81	52	129	63	89	36	94	59
Brain	89	65	72	49	45	71	68	43	76	59
CB2-30%	265	102	297	54	335	54	293	39	282	74
Cortical Bone	666	83	696	53	704	57	706	38	609	77
Adipose	-54	101	-43	48	-25	61	-45	37	-101	90
M1 (Steel)	5255	103	x	x	5132	115	x	x	5218	76
M2 (Steel)	5143	103	x	x	5125	104	x	x	5121	80
Aluminum	1307	56	x	x	1295	61	x	x	1276	52
Lead	8405	122	x	x	8078	149	x	x	8289	113

Table 3.3: The mean MVCT numbers of the various tissue equivalent and metal plugs and their standard deviations. Arrangements with 'No Metal' were imaged with all metal plugs removed.

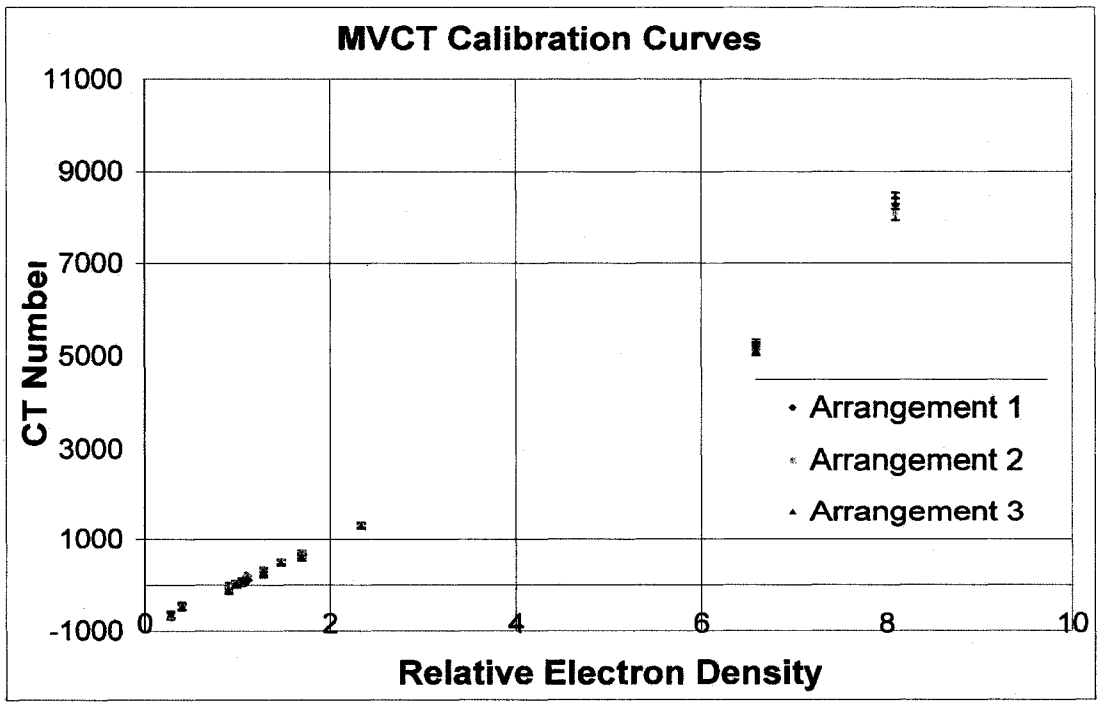

Figure 3.4: Calibration curves measured for the three plug arrangements. These curves include the metal plug data.

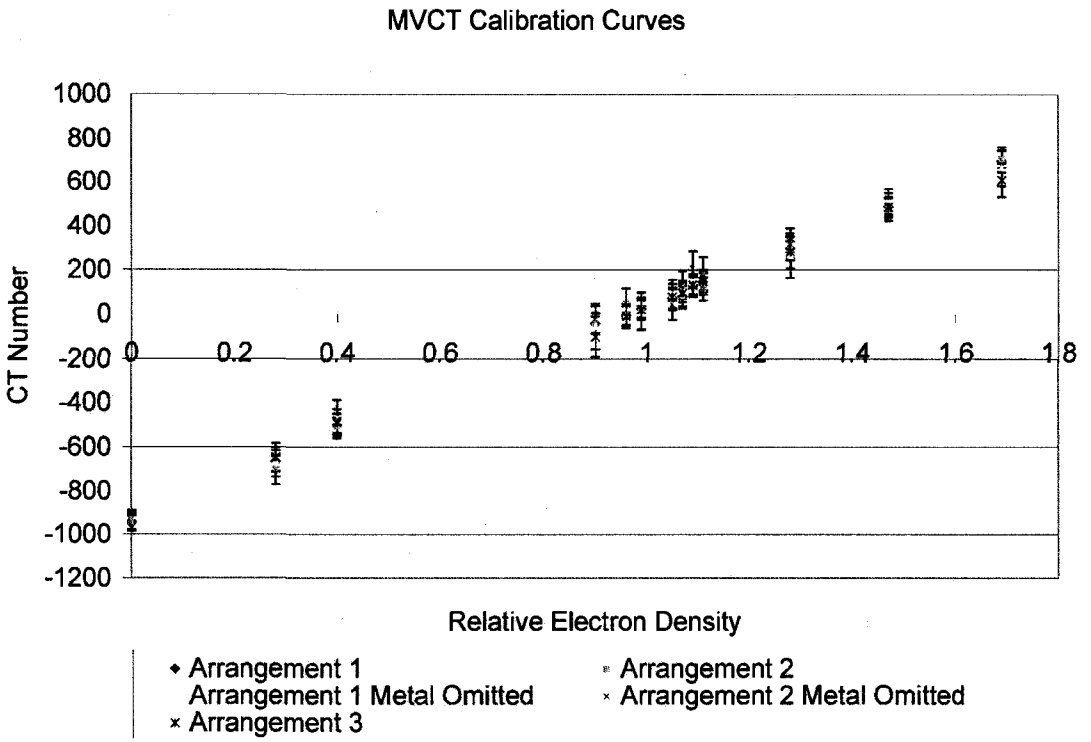

Figure 3.5: A blow up of the normal tissue region of the curve. Metal plug data is not shown in this plot.

As can be seen from the calibration curves in Figure 3.4 and Figure 3.5, the calibration curves are not affected appreciably by plug depth or phantom displacement. A closer look at the average CT numbers in Table 3.3 measured for the plugs reveals that the values measured in the five sets of images are equal to each other within error in all cases except for lead, which has a higher atomic number and density than any of the three alloys currently used in hip prostheses. This is likely the result of beam hardening, as evidenced by the decrease in CT number from 8405 to 8078 with increasing depth of plug placement.

The fact that all points agree within experimental error under plug rearrangement and phantom displacement indicates that the MVCT numbers can be reliably converted to electron density for use with heterogeneity corrections. This confirms previous work by Langen et al who found that "use of MVCT images for dose calculations can be accomplished with an accuracy that is similar to that of dose computations in kVCT

images" [23]. The data taken with Arrangement 1, including metal, was chosen as the calibration curve which was entered into the Eclipse treatment planning system. This curve can be seen in Figure 3.6, along with a straight line fit to the data for points up to and including steel, its equation, and the Pearson product-moment correlation coefficient (R^2) which measures the goodness of fit. The closer the value is to unity, the better the fit to the data. The value calculated for our data, $R^2 = 0.9997$, is very close to unity, indicating a very good fit to the data. The larger standard deviations associated with the metal plugs is likely the result of a cupping artifact due to beam hardening, where the numbers towards the center of the metal plugs are lower than towards the edges.

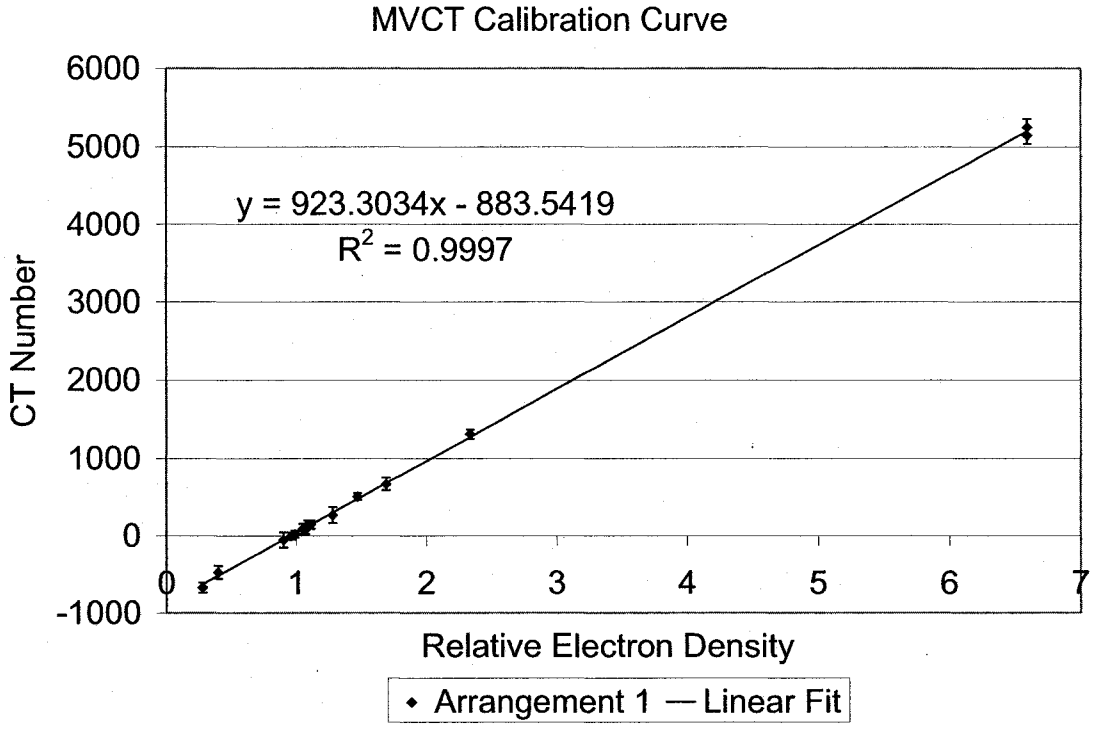

Figure 3.6: The curve used for conversion of MVCT numbers to electron densities for use in heterogeneity corrections in the Eclipse treatment planning system.

3.3.2 kVCT Calibration Measurements

The measured values for the mean CT number for each plug, along with its standard

deviation for the scan with metal absent can be seen in Table 3.4. A plot of the mean CT number versus the relative electron density is shown in Figure 3.7. Shown on the plot are two separate linear fits to the data points above a relative electron density of 1 and to the points below a relative electron density of 1. This is done clinically because the human body is largely made up of water equivalent tissues (e.g. fat, water, soft tissue) and bone (e.g. compact bone, cortical bone), with a higher density and effective atomic number. MVCT numbers measured for different tissues therefore tend to fall on one of two lines.

Material	Weighted Mean CT Number	Standard Deviation of the Weighted Mean
Air (M1)	-958	13
Air (M2)	-955	15
Air (M3)	-960	13
Air (Pb)	-958	14
CB2-50%	818	19
Bone	232	15
Solid Water	8	14
Breast	-35	16
Inner Bone	226	17
Lung I	-530	19
Lung II	-695	16
Liver	73	17
Brain	30	16
CB2-30%	446	19
Cortical Bone	1210	19
Adipose	-87	16

Table 3.4: Measured mean CT numbers and their standard deviations for the images with metal absent.

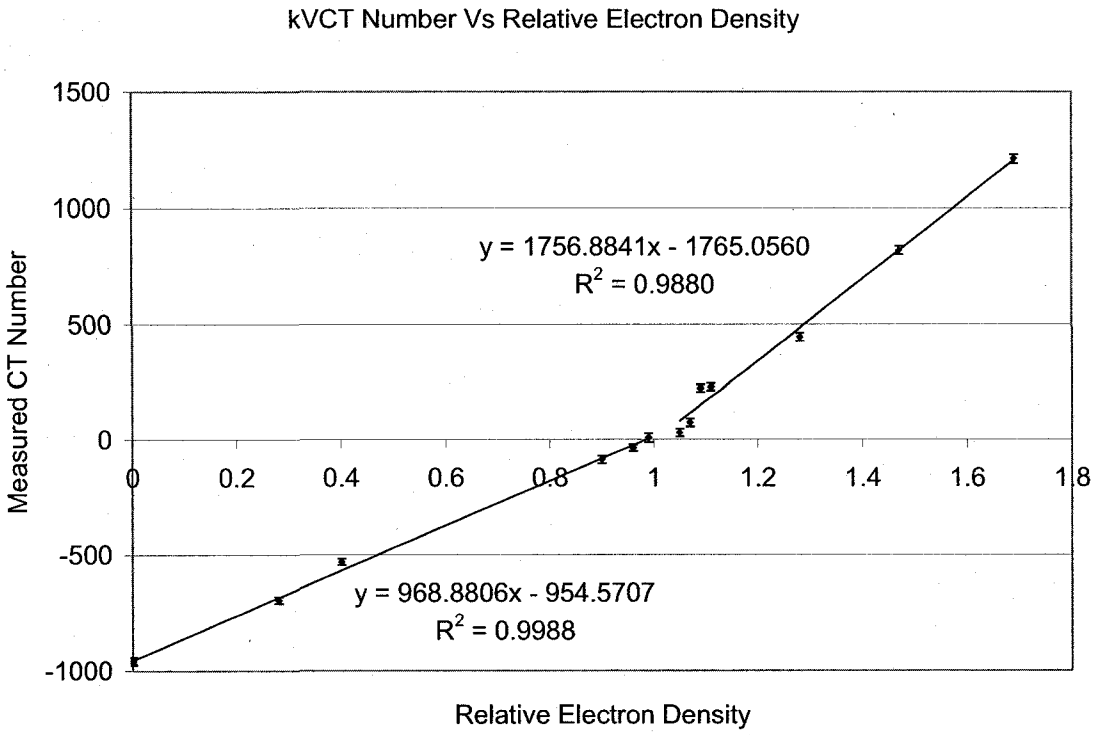

Figure 3.7: Plot of the measured mean kVCT numbers vs relative electron density.

3.3.3 Comparison of Metal Artifacts in kVCT and MVCT Images

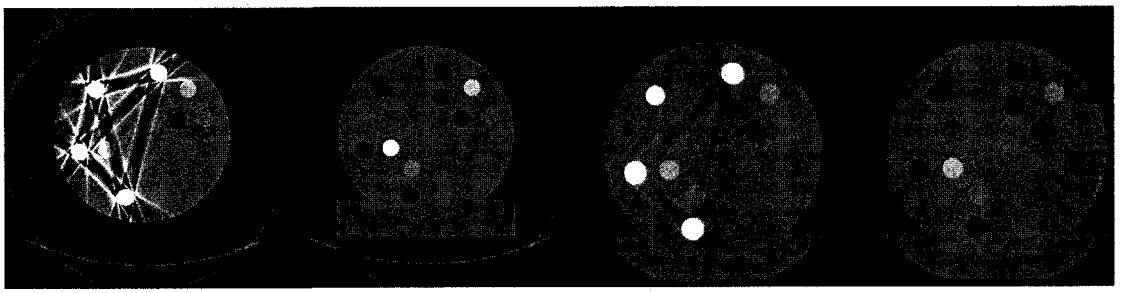

(a) *(b)* *(c)* *(d)*

Figure 3.8: The four pictures show CT scans of the cheese phantom with and without metal plugs. All scans are shown with a level of 0 and a window of 2000. (a) kVCT with metal (b) kVCT without metal (c) MVCT with metal (d) MVCT without metal.

The images taken for calibration purposes were also used to investigate the effect of metal artifacts on the measured kVCT and MVCT numbers by comparing the images

taken with and without the metal plugs. This was done for plug arrangement 1. Sample images can be seen in Figure 3.8.

Qualitatively it is clear that the metal artifacts are less prominent in the MVCT image containing metal than in the kVCT image containing metal. This indicates that non-linearities such as beam hardening and photon starvation, discussed in 2.7.2.2, are mitigated by the greater energy of the MV photons. ROIs were again drawn over the plug locations (as explained in 3.2.2.1) and the mean and standard deviation of each ROI was calculated. The values for non-metal plugs are listed in Table 3.5 and Table 3.6 below.

kVCT	No Metal		With Metal	
	Mean	Std. Dev.	Mean	Std. Dev.
CB2-50%	819	38	704	82
Bone	233	28	243	61
Solid Water	8	26	-12	65
Breast	-37	27	3	62
Inner Bone	222	28	302	87
Lung I	-532	32	-426	365
Lung II	-694	32	-566	61
Liver	74	28	44	71
Brain	29	27	60	84
CB2-30%	442	31	558	429
Cortical Bone	1204	34	919	464
Adipose	-85	31	-475	565

Table 3.5: The mean kVCT numbers and their standard deviations measured for plugs in images with and without metal.

MVCT	No Metal		With Metal	
	Mean	Std. Dev.	Mean	Std. Dev.
CB2-50%	487	39	508	45
Bone	142	37	134	59
Solid Water	22	39	26	45
Breast	-10	41	-3	52
Inner Bone	122	39	134	55
Lung I	-492	51	-442	84
Lung II	-668	49	-663	65
Liver	93	48	76	61
Brain	84	48	77	62
CB2-30%	298	54	231	99
Cortical Bone	695	50	672	75
Adipose	-42	48	-57	107

Table 3.6: The mean MVCT numbers and their standard deviations measured for plugs in images with and without metal.

There are four plugs which have a streak artifact lying across them. These are highlighted in yellow in Table 3.5 and Table 3.6. The standard deviation of the mean CT numbers increases by an order of magnitude or more for kVCT scans, while they only increase by a factor of 2 for MVCT. In order to compare the dosimetric effect resulting from a change in CT number between the kVCT and MVCT image sets, the CT numbers must first be converted to electron densities. Comparison of the numbers themselves is meaningless because they are used in conjunction with different conversion curves for calculation purposes. In other words, an equal change in CT number will not affect dose calculations in the same way for the two image sets. The CT numbers were converted to an electron density relative to water using the curves measured in 3.3.1 and 3.3.2. The results can be seen in Table 3.7.

Plug Material	Change in Apparent Electron Density (relative to water)	
	kVCT	MVCT
Lung I	0.12	0.06
CB2-30%	0.07	0.07
Cortical Bone	0.17	0.03
Adipose	0.43	0.02

Table 3.7: Changes in electron density in different plugs affected by metal artifacts.

In the worst case (adipose tissue), the change in measured electron density is 21 times larger in the kVCT images than in the MVCT images. In the best case, the change in bone (CB2-30% mineral) is the same, even though the CT numbers change considerably more for the kVCT images. This is due to the broken nature of the kVCT calibration curve, which, for densities higher than water, becomes less sensitive to changes in CT number. The MVCT curve has a single slope up to an electron density of steel and therefore does not exhibit this behaviour. The cortical bone plug on the other hand still changes far more for kVCT than MVCT, despite the conversion becoming less sensitive for kVCT. It would be fair to say that in regions affected by metal artifacts kVCT will perform equal to MVCT at best in a minority of cases, while for the majority MVCT will outperform kVCT in measuring accurate electron densities for use in heterogeneity corrections in the presence of metal. The position and proximity of the region of interest to a metal prosthesis will determine to a large extent how beneficial MVCT images will be in measuring accurate CT numbers.

Measured kVCT and MVCT numbers for the metal plugs may also be compared to theoretical values. kVCT values for metal plugs can be seen in Table 3.8, along with calculated values for comparison.

Material	Attenuation Coefficient (μ) (1/cm)	Calculated CT Number	Measured CT Number	Standard Deviation (Measured)
Lead	73.32	338449	6032	1061
Aluminum	0.87	3011	6167	1407
Stainless Steel	12.21	55538	6697	1797

Table 3.8: Calculated and measured kVCT numbers for Al, Pb and Fe.

For the kVCT beam, its half value layer in aluminum (8mm) was used to find its equivalent photon energy, or the energy of a monoenergetic beam which can be used to approximate the behaviour of the polyenergetic beam [25]. The equivalent energy was then used with the NIST XCOM database to find attenuation values in the various metals and in water. These values were then used in equation (2.1) to calculate approximate CT numbers for the metals. A more sophisticated calculation, like that carried out for the MVCT numbers, was not possible as the beam spectrum for the kVCT unit was not available.

The measured kVCT numbers for all three metals are equivalent within error, despite the fact that aluminum is roughly 4 times less dense than lead in terms of mass. This is the result of photon starvation. The measured intensity, dominated by scatter and noise rather than transmitted photons, reaches some minimum value and the CT numbers assigned no longer reflect the attenuation of the voxel. This is also why measured kVCT values do not correspond to the theoretical numbers which should be assigned, which is consistent with what we would expect. For aluminum, we have a measured number that is higher than the calculated number, whereas for the other metals the measured number is lower. This is likely due to the presence of the other metal plugs, and the overlapping of multiple artifacts. In order to verify this the plugs could be scanned one at a time inside the phantom, so that no interference would occur.

Calculated and measured MVCT numbers for metals can be seen in Table 3.9.

Material	Attenuation Coefficients (1/cm)		Calculated CT Numbers		Measured CT Numbers	
	Before Hardening	Hardened	Before Hardening	Hardened	CT #	Standard Deviation
Lead	0.78	0.58	10252	7301	8358	126
Aluminum	0.16	0.15	1346	1102	1303	55
Stainless Steel	0.47	0.41	5722	4834	5268	105

Table 3.9: Calculated and measured MVCT numbers for Al, Pb and Fe.

For the MVCT beam, values for μ were found using the approximation that the polyenergetic beam can be treated as a monoenergetic beam with an energy equal to the average energy of the polyenergetic beam. The average energies used for the MVCT beam were found using a beam spectrum provided by Dr. Marc Mackenzie. This spectrum was obtained from a Monte Carlo simulation. The spectrum was split into bins of width 0.08 MeV and each bin contained a fraction of the total number of photons generated in the beam. In order to account for beam hardening, two average beam energies were found for each metal. The first was the average energy of the beam before it entered the phantom, and the second was the average energy of the beam after penetrating half the diameter of the solid water phantom (15cm) and half the metal plug diameter (1.4cm). These energies were then used to find values for μ for each metal and for water using the NIST XCOM Database [31] which were used with equation (2.1) in order to calculate the maximum and minimum CT numbers theoretically achievable.

The measured MVCT numbers are well separated from each other, and have a much smaller standard deviation associated with them making them more precise than measured kVCT numbers. The measured MVCT numbers also fall between the MVCT numbers calculated for the two average beam energies. This signifies that the measured MVCT numbers are consistent with calculations, as the two calculated values represent extreme values, and so should bracket the measured MVCT number. The MVCT numbers are therefore more suitable for use in dose calculations than kVCT numbers for inhomogeneity correction.

3.4 Summary

We have confirmed that the CT number-to-electron density calibration curve for the TomoTherapy unit, working in imaging mode, is not dependent on plug arrangement or phantom positioning, as previous work had suggested [23]. Average CT numbers for each tissue equivalent or metal plug, scanned at different depths and placements, were the same to within experimental error except in three cases. In two cases the presence of a metal artifact directly overlapping the plug in one arrangment, but not the other two, caused this discrepancy. The third discrepancy was due to the extremely high density and atomic number of the plug (Pb in this case). A suitable CT number-to-electron density calibration has been obtained for later use. We have also shown that in a solid water phantom, MVCT images are less affected by the presence of metal artifacts both qualitatively and quantitatively. This indicates that MVCT images may offer some advantages over kVCT images for both delineation of critical structures affected by metal artifacts and for dose calculations. We have also shown that kVCT numbers for metals are not consistent with calculations and imprecise since they become saturated, even in the case of aluminum. Measured kVCT numbers for different metals are incorrectly equal to within error, despite a mass density difference of 4 between aluminum and lead. The measured values are not equal to calculated values to within experimental error. MVCT numbers for all metals on the other hand remain well spaced with small standard deviations in comparison with kVCT values, and are equal to calculated values to within experimental error. The next step is to assess the clinical impact of using MVCT images and the CT number-to-electron density calibration table in the calculation of dose distributions for prostate cancer patients with hip prostheses.

Chapter 4: Comparison of kVCT and MVCT Images in Treatment Planning

4.1 Objective

The objective of this chapter is to compare the use of clinical MVCT and kVCT image sets:

1. For target delineation of the prostate, and
2. For clinical dose calculation for a typical prostate treatment setup.

The work of Chapter 3 has shown that MVCT images can be reliably calibrated for use in treatment planning, and are superior to kVCT images in approaching the correct electron densities in the presence of metal. The actual clinical impact of these findings are assessed. Images from an ethics approved Image Guided Adaptive Radiotherapy (IGAR) imaging study that involved kVCT and MVCT imaging of the pelvic region of patients with hip prostheses are used by four physicians for contouring the prostate. The volumes drawn are analyzed in order to identify the superior imaging modality. The kVCT and MVCT images of one of these patients are then used for dose calculations, in order to compare the differences between the calculations.

4.2 Methods and Materials

4.2.1 Materials

The list of materials used in this portion of experiments can be seen in Table 4.1. A short description of each piece follows.

Item	Description	Manufacturer / Supplier
Eclipse TPS (v 6.5 & v 7.5)	The treatment planning system used in the Cross Cancer Institute.	Varian Oncology Systems, Palo Alto, CA.
4 MVCT and 4 kVCT Image Sets of Patients with Hip Prostheses	Image sets originally taken for an ethics approved IGAR imaging study (IGAR 2003-I1, CCI Ethics # 21131)	Cross Cancer Institute

Table 4.1: The list of materials used for the comparison of kVCT and MVCT images in treatment planning for patients with metal hip prostheses.

4.2.1.1 Eclipse Treatment Planning System

In this work, the Eclipse TPS (v6.5 and v7.5) (Varian Oncology Systems, Palo Alto CA) was used, which utilizes the Anisotropic Analytical Algorithm (AAA). Two versions were available for use: version 7.5.18, currently in clinical use, and its eventual successor, version 8.0.5. The AAA algorithm is a 3-dimensional pencil beam convolution/superposition algorithm that uses Monte Carlo models of dose deposition of pencil beams in water, called kernels, to calculate dose in patients. The name of the algorithm stems from the fact that most of the convolution operators appearing in the mathematical formalism may be converted into analytical expressions and that the AAA accounts for tissue heterogeneity anisotropically in the 3D neighbourhood of an interaction site by using photon scatter kernels in multiple lateral directions. The final dose distribution is obtained by the addition of photon and electron convolutions [32]. The algorithm itself is divided into two separate subalgorithms: the configuration algorithm and the dose calculation algorithm. The configuration algorithm determines the fundamental physical parameters needed for dose calculation, such as the photon energy spectrum and the mean radial energy, and it subdivides broad beams into individual finite-sized beamlets. The clinical beam is divided into three components: the primary photon energy fluence, the extra-focal photon energy fluence (ie photons not coming directly from the target), and the contaminant electron fluence. The global

model is based on the use of multiple sources for each of the three components.

The dose calculation is based on the convolution over the beamlets of the three radiation components separately using the parameters defined for every beamlet. The superposition of the individual beamlet contributions yields the complete dose distribution. Tissue heterogeneity is taken into account with an anisotropic approach based on the application of six independent exponential absorption functions to model lateral energy scaling of pencil beams. This is done in the six different directions $\pm x, \pm y, \pm z$ [32].

4.2.1.2 MVCT and kVCT imaging studies

In a previous ethics approved imaging study (IGAR 2003-I1, CCI Ethics # 21131), ten patients were accrued to a study designed to look at the effects of metal implants on MVCT and kVCT imaging. The patients had implants in varying regions, summarized in Table 4.2. Each patient had both a diagnostic CT scan followed by a MVCT scan directly following. The scans were taken as closely together in time as possible to minimize changes in anatomy due to bladder and rectal filling.

Metal Implant	Number of Patients
Pelvic Bolt	1
Single Hip Prosthesis	3
Dual Hip Prostheses	1
Spine Implant	1
Knee Replacement	2
Gold Seed Implants	2

Table 4.2: Implant types of patients accrued to MVCT imaging study.

4.3 Target Delineation on kVCT and MVCT Clinical Studies

The kVCT and MVCT image sets of the four patients possessing hip prostheses were used to compare the delineation of the prostate in close proximity to metal. Four physicians were recruited to contour the prostate of each patient, in both the kVCT and MVCT image sets, resulting in eight volumes per patient. The contours were drawn with the contouring workspace tools included in Eclipse v6.5. The original image sets

were duplicated for each physician, so that each physician delineated the prostate volumes completely independently. A fifth image set was created for each kVCT and MVCT study. The four physician contours for each imaging modality were gathered together on this fifth set for analysis. Volume measuring tools included in Eclipse were used for this purpose, and with Microsoft Excel (Microsoft Corporation, Redmond, WA) the average volumes among physicians along with their standard deviations were calculated. Since the real size and shape of the prostates are unknown, the average volume and its standard deviation, along with the overlapping volume as a fraction of the average have been used to identify the superior modality. If one image modality consistently has larger average volumes, this may indicate an inferior modality as the size of contours increase as uncertainty about the location of the structure increases. A larger standard deviation would indicate greater disagreement between physicians as to the size of the prostate. Lastly, a smaller overlapping volume, or volume common to all four contours, would indicate higher disagreement between physicians regarding the location of the prostate, as well as its size. If one image modality consistently demonstrates smaller average volumes, lower standard deviations and greater overlapping volumes, a strong argument can be made for its superiority. The final criterion which was used as an indicator is the opinion of the physicians, though it is subjective in nature.

4.4 Dose Calculations with kVCT and MVCT Studies

One of the single hip prosthesis patients was used in order to quantify differences when calculating dose distributions using kVCT images versus MVCT images. The prostate contour drawn by the most experienced physician was used and contours of the rectum and bladder were added with the aid of a cross-sectional anatomy guide [33]. These contours were later checked by a physician to ensure that they were accurate.

Dose calculations were carried out using the Eclipse AAA algorithm (v. 7.5.18) on both the kVCT and MVCT image sets. The kVCT images had CT numbers capped at 3095 as a result of being transferred first to a virtual simulation system that automatically caps CT numbers. MVCT numbers were not capped. A four field technique was used to treat

the entire prostate in both image sets, with 15MV beams at 0°, 90°, 270° and 180°. The beam arrangement was chosen in order to observe the maximum error associated with the use of kVCT images since they are unable to yield accurate CT numbers for metal. It should be noted that this setup is only being used for demonstration purposes in this work and is not the setup that would be used clinically. A clinical setup would avoid treating through the prosthesis as much as possible. The anterior-posterior and posterior-anterior beams (located at 0° and 180°) had beam weights of 0.3, while the lateral beams (90°, 270°) had beam weights of 0.2. Each beam used a multileaf collimator to shape the field to the shape of the PTV, with margins of 0.7 cm in the anterior, posterior and lateral directions and 1.0 cm in the superior and inferior directions. The setup can be seen in Figure 4.1. The treatment plan generated included 35 fractions of 200 cGy per fraction, yielding a total dose of 70 Gy to the centre of the prostate.

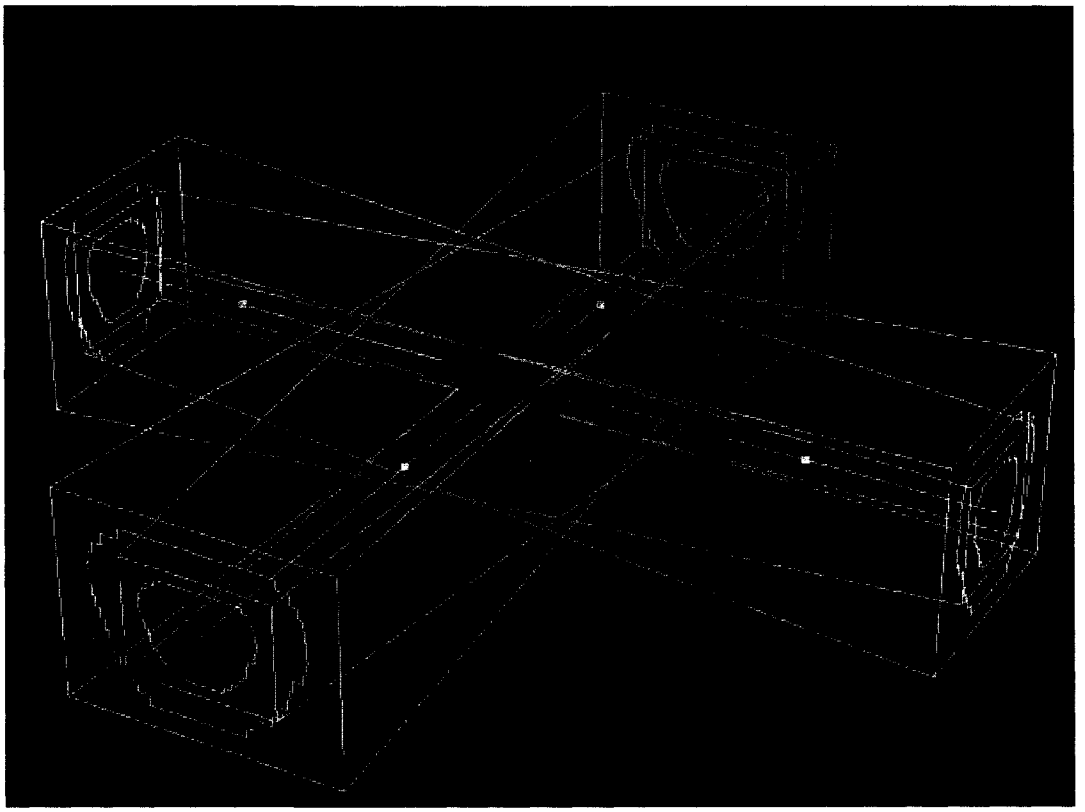

Figure 4.1: The beam arrangement used for comparison of treatment plans generated using MVCT and kVCT images. Shown in the figure are the body contour, the PTV, the metal implant and the hip socket. Also shown are the beams used and the projection of the PTV and the MLC contour.

Once dose distributions had been calculated on the images separately, the images were fused using the automatic image registration algorithm included in the Eclipse TPS. Fused images were inspected visually to ensure that there were no gross errors. No detailed analysis of the registration algorithm was carried out. The dose distribution calculated using the kVCT images was then subtracted from the dose distribution calculated using the MVCT images, and the dose difference distribution was displayed as a dose colour wash overlaid on the kVCT image set.

4.5 Results and Discussion

4.5.1 Target Delineation Results

Sample images of the contours of the prostate in both MVCT and kVCT images are

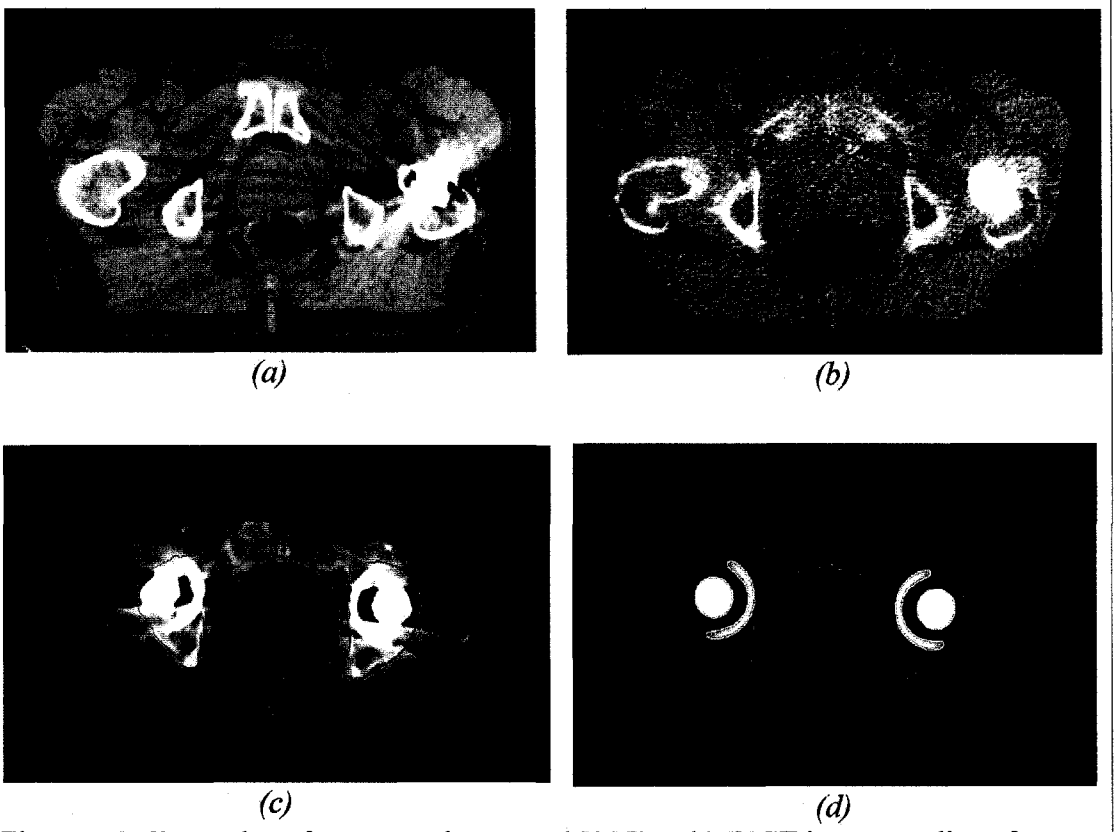

Figure 4.2: Examples of contours drawn on kVCT and MVCT image studies of patients with metal hip prostheses. Windows and levels are those automatically chosen by Eclipse, and so are not the same. (a) kVCT, single hip prosthesis (b) MVCT, single hip prosthesis (c) kVCT, Dual hip prostheses (d) MVCT, Dual hip prostheses.

shown in Figure 4.2. The results of the analysis of the 32 volumes drawn for the four patients possessing hip prostheses can be seen in Table 4.3, Table 4.4, Table 4.5 and Table 4.6.

Single Hip Implant Patient 1 (left side)					
	Prostate Volumes (cm^3)			Overlapping Volume (% of Average)	Physician's Opinion
	Average Volume	Std. Dev.	Overlapping Volume		
MV	75.44	20.55	24.78	32.85%	Inferior
kV	52.75	7.91	37.69	71.45%	Superior

Table 4.3: Statistics on prostate volumes drawn for single hip implant patient 1.

Single Hip Implant Patient 2 (left side)					
	Prostate Volumes (cm^3)			Overlapping Volume (% of Average)	Physician's Opinion
	Average Volume	Std. Dev.	Overlapping Volume		
MV	67.51	7.22	48.56	71.93%	Inferior
kV	55.01	7.50	28.67	52.12%	Superior

Table 4.4: Statistics on prostate volumes drawn for single hip implant patient 2.

Dual Hip Implant Patient					
	Prostate Volumes (cm^3)			Overlapping Volume (% of Average)	Physician's Opinion
	Average Volume	Std. Dev.	Overlapping Volume		
MV	60.78	28.54	19.20	31.59%	Superior
kV	57.56	13.68	24.06	41.80%	Inferior

Table 4.5: Statistics on prostate volumes drawn for the dual hip implant patient.

Single Hip Implant Patient 3 (right side)					
	Prostate Volumes (cm^3)			Overlapping Volume (% of Average)	Physician's Opinion
	Average Volume	Std. Dev.	Overlapping Volume		
MV	69.19	15.40	35.51	51.32%	Inferior
kV	42.53	2.48	18.51	43.52%	Superior

Table 4.6: Statistics on prostate volumes drawn for single hip implant patient 3.

As can be seen from the tables, the average volumes were larger in the MVCT images for all patients. The standard deviation was larger for MVCT images in 3 of 4 patients. The overlapping volumes as a percentage of the average volume were larger for MVCT images in 2 of the 4 cases. The physicians all agreed that the prostate was easier to delineate in the kVCT images for single prosthesis patients, while for the dual hip prosthesis patients the prostate was easier to delineate using MVCT images. Given a rather small sample size, the data indicates that kVCT images offer some advantage for use in contouring prostates, especially for single hip implants. The data is somewhat contradictory however, since, for example, the physicians all preferred MVCT for the dual hip implant case, and yet the average volume and its associated standard deviation

were larger for the MVCT images and the overlapping volume as a percentage of the average was smaller. This may be a result of the lack of data in the kVCT images, since the lack of data also means a scarcity of ways of interpreting it, resulting in greater consistency. In light of this, if there is a superior modality for imaging patients with prostates and hip prostheses, further investigation is needed to identify it.

4.5.2 Dose Calculation Results

The dose distribution difference is shown in Figure 4.3. The difference caused by the use of incorrect CT numbers for the prosthesis in the kVCT images is apparent (outlined in Figure 4.3), but the difference is only 1Gy out of 70 Gy. Other regions located around the body contour and the edge of the beams have differences larger than that due to the implant. These differences are caused by slight differences in patient geometry.

Figure 4.3: Dose difference distribution between treatment plans generated with MVCT and kVCT images. The difference due to the metal implant is outlined by the black box.

The difference in calculated doses in the shadow of the prosthesis is roughly 1 Gy. This represents a difference of only 1.4% for a treatment prescription of 70 Gy. This is approaching clinical irrelevance, despite the fact that the kVCT numbers have been

capped at 3095, corresponding to an electron density of roughly 2.3 times that of water. The MVCT numbers for the metal prosthesis yield an electron density closer to 6.6 times that of water.

These results can be contrasted with the results of the simulations of Ding et al [34] that for a typical four field box treatment of a water phantom with two 2 cm thick slabs of steel shielding the two lateral beams the dose predicted by Monte Carlo is 13% lower than that predicted by CadPlan, the precursor to Eclipse. Though the algorithms are different, the primary shortcoming of both calculations is the same. In Ding's case, CadPlan capped electron densities at 2.0 relative to water, which is the primary reason for its poor performance in the presence of metal according to Ding. In our case the kVCT images contain CT numbers capped at 3095. We should therefore expect roughly half the dose difference between treatment plans generated with MVCT images and kVCT images as Ding found between treatment plans generated with Monte Carlo and CadPlan if treatment plans generated with Eclipse using MVCT images are accurate. Since there are not significantly large differences between the dose distributions calculated from kVCT images with capped, corrupted CT numbers and dose distributions calculated from MVCT images with CT numbers that accurately reflect electron density, the ability of the Eclipse AAA dose calculation algorithm to accurately calculate dose in the presence of high electron density inhomogeneities is brought into question. The use of MVCT images for treatment planning for patients with metal implants in our clinic will offer little to no benefit if Eclipse cannot accurately calculate doses in the presence of metal. This requires further investigation, which is the purpose of Chapter 5.

4.6 Summary

We have been unable to definitively identify the superior imaging modality for contouring the prostate when hip prostheses are present, although the average prostate volumes, their standard deviations and the opinion of the physicians may indicate that kVCT imaging has a slight advantage, especially for patients with only one prosthesis.

Dose calculations carried out with both kVCT and MVCT image sets for a four field box

treatment of a prostate in a patient with a single hip prosthesis unexpectedly showed very little difference between the calculations. In the shadow of the prosthesis, the dose difference was roughly 1 Gy for a prescription dose of 70 Gy to the centre of the prostate. This represents a difference of only 1.4% of the prescription dose, much smaller than the expected ~6% given that the kVCT numbers of the prosthesis were capped at 3095, corresponding to an electron density relative to water of 2.3. The MVCT numbers for the prosthesis on the other hand corresponded to a relative electron density of 6.6, nearly three times as large.

Chapter 5: Dose Calculation Accuracy with Metal Prostheses

5.1 Objective

The objective of this chapter is to assess the accuracy of the Eclipse AAA algorithm in calculating doses in the presence of metal. This is required to confirm that Eclipse is capable of accurate dose calculations if given high electron density information. The results of the previous chapter have cast doubt on this assumption. A patient possessing a single hip prosthesis is simulated by a water tank and a metal rod. The dose distribution resulting from the application of a single lateral beam of a typical clinical field size is measured. The phantom is then scanned in the MVCT unit and planned using the Eclipse TPS and AAA algorithm. Monte Carlo calculations are also carried out for comparison. The calculated dose distributions are then compared to the measurements to assess the accuracy of the Eclipse AAA algorithm.

5.2 Methods and Materials

5.2.1 Materials

The list of materials used in this portion of experiments can be seen in Table 5.1. A short description of each piece follows.

Item	Description	Manufacturer / Supplier
Scanditronix Wellhofer Scanning Apparatus	Apparatus capable of. measuring dose distributions in a water tank	Scanditronix Wellhofer North America, Bartlett, TN
In-house Water Tank	A water tank capable of fitting into the MVCT bore	Cross Cancer Institute
Steel Rod and holder	Rod used to simulate a typical hip prosthesis.	Goodfellow Corporation, Oakdale, PA (Rod) Cross Cancer Institute (holder)
EGSnrc Monte Carlo Dose Calculations	Monte Carlo dose calculations of the water tank and steel rod phantom for comparison to Eclipse dose calculations.	Charles Kirkby, Cross Cancer Institute, EGSnrc
TomoTherapy HI·ART II treatment delivery system	The TomoTherapy system can be used in imaging mode as a MVCT unit.	TomoTherapy Inc., Madison, WI, USA
Varian Clinac 2100EX linear accelerator	A linear accelerator capable of producing both photon and electron beams of various energies.	Varian Inc., Palo Alto, CA, USA

Table 5.1: Materials used in the assessment of the dose calculation accuracy of the Eclipse TPS in the presence of metal.

5.2.1.1 Scanditronix Wellhofer Scanning Apparatus

A Scanditronix Wellhofer Blue Phantom scanning apparatus (Scanditronix Wellhofer North America, Bartlett, TN) was used to measure dose in water in the proximity of a steel rod. A diagram of the apparatus is shown in Figure 5.1. The scanning apparatus consists of a tank with 15mm walls and bottom made of Perspex with a scanning volume of 480 x 480 x 480 mm^3. Rails are fitted to the sides of the tank which permit an ionisation chamber to scan throughout the volume of the tank. Precision DC motors control the scanning motion with a position accuracy of +/-0.8mm per axis, a reproducibility of +/-0.1mm and an orthogonality of +/- 0.2 degrees [35]. A control unit, the Scanditronix Wellhofer CU500E, provides the link between the scanning apparatus (motors and ionization chambers) and a personal computer for entering commands and

displaying and analyzing measurements. The computer can be used to queue a number of measurements to be done sequentially, so that in our case a number of profiles could be obtained without any input from the user after initial setup to map the dose distribution behind the rod.

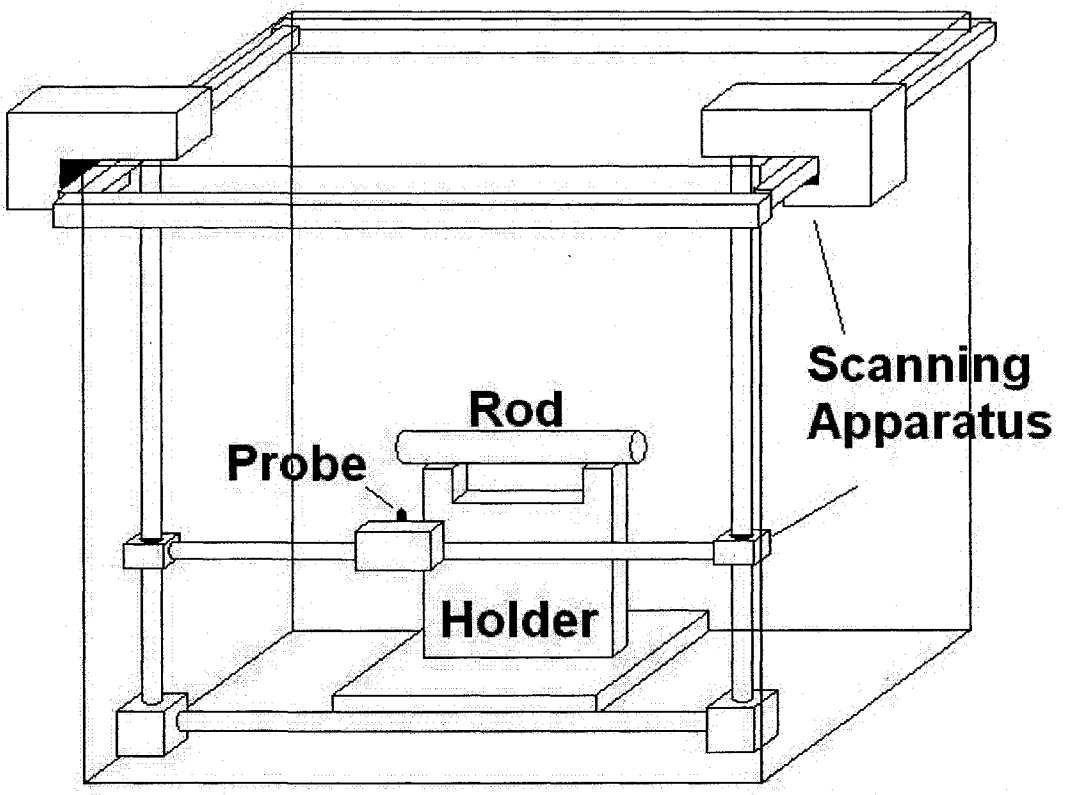

Figure 5.1: Diagram of the Scanditronix Wellhofer Blue Phantom and scanning apparatus used to measure the dose distribution behind a stainless steel rod.

5.2.1.2 In-house Water Tank

The Wellhofer Blue phantom is too large to fit into the TomoTherapy bore. A second, smaller phantom was used to obtain MVCT scans of the steel rod and holder immersed in water. The walls were made of clear plastic and the tank measured 40×40×40 cm^3.

5.2.1.3 Stainless Steel Rod and Holder

The rod used to simulate a hip prosthesis was fabricated from stainless steel 316L, which is one of the alloys used for prostheses and its properties were listed in Table 2.2. The rod had a 2.85cm diameter and 15cm length. The diameter of the rod was made equal to a measurement of the diameter of the femoral head of a hip prosthesis of one of the patients accrued to the IGAR imaging study. The holder used with the rod was made of clear plastic, and when pushed against the inner wall of the water tank held the rod at a depth of 9.4cm, also equal to the lateral depth of an actual implant in one of the patients in the IGAR imaging study. The rod and holder can be seen in Figure 5.1 inside the Wellhofer scanning apparatus.

5.2.1.4 Monte Carlo Dose Calculations

Dr. Charlie Kirkby carried out Monte Carlo dose calculations using the MVCT images of the in-house water tank containing the steel rod. All of the work involved in obtaining these calculations was carried out by him, using software developed by the National Research Council, called Electron Gamma Shower (EGSnrc) [36].

DICOM RT data objects associated with the original treatment plans created in Eclipse were exported to a dedicated Monte Carlo workstation. The data objects included the following:

1. DICOM RT plan, which contains geometric and dosimetric data such as external beam components.
2. DICOM RT structure set, which contains data related to anatomy such as contour information.
3. DICOM RT dose, which contains data pertaining to dose distributions such as reference points and isodose curves, as well as the 3D dose matrix.
4. The CT image set.

A sequence of EGSnrc-based [36] user codes were run on a parallel computing cluster based on information obtained from the DICOM RT objects. The EGSnrc-based codes

were run using an in-house MATLAB (Mathworks Inc., Natick, MA) code. The cluster used in the simulations consisted of 48 2.0 GHz 64 bit Opteron246 processors (AMD, Sunnyvale CA).

The program BEAMnrcMP [37][38] was used to model the accelerator head, while DOSXYZnrc [39] was used to calculate doses in the 3D volumes imported from Eclipse. The parameters used in the BEAMnrcMP simulations were obtained from the technical specifications for a Varian 21EX linac, provided by Varian (Varian Oncology Systems, Palo Alto CA). Suitable characteristics of the electron beam for the 21EX, such as mean energy and energy spatial distribution incident on the target, had been found in the earlier work of Bagheri and Rogers for a 15 MV beam [40]. The minimum energy threshold values for the creation of secondary Bremsstrahlung photons and knock-on electrons, AP and AE respectively, and for the continued tracking of photons and electrons by the code, PCUT and ECUT, were set to AP = PCUT = 0.01 MeV and AE = ECUT = 0.7 MeV. The simulation of the linac head was split into three separate phases: the stationary components of the linac head which exist as an archived phase space, the jaws, and the parked MLC and other beam-shaping devices set to air for this work. Electron range rejection was used with a cut-off (ESAVE_GLOBAL) of 2.5 MeV for simulation through the secondary collimation jaws. Differences in depth dose curves for standard 10x10 cm fields using this technique were less than 1% of the maximum dose. The output of the BEAMnrcMP simulation, stored as a phase space, were used by the DOSXYZnrc simulations as the radiation source located 70cm from the target. An absolute calibration similar to the type described by Popescu et al was used [41], differing only slightly in the accounting of the monitor unit ion chamber backscatter dose due to the jaws. We created a lookup table based on field size, dispensing with the need to read this value in during the automated simulation. The DOSXYZnrc simulation ran a total of 660M histories for the dose calculations which consisted of roughly 16.5M unique particles with 40 times recycling. The results were not filtered.

The 3D voxelized phantom representation of the setup was developed from a set of MVCT images imported from Eclipse. An in-house version of the BEAMnrc software,

CTcreate, was used for this purpose and allowed for the use of both kVCT and MVCT images. Mass densities and materials based on an array of modified CT numbers were used to define an ".egsphant" file. The modified CT number (h') is related to the traditional CT number (h) by [42]:

$$h' = \frac{h + 1000}{1000} \qquad (5.10)$$

The calibration measurements described in Section 3.4 were used to establish a MVCT number (h') to mass density (ρ) conversion given by:

$$\rho = \begin{cases} 0.001 & h' < 0.08 \\ h' \times 1.0643 - 0.0770 & 0.08 \geq h' < 1.00 \\ h' \times 1.2717 - 0.2767 & h' \geq 1.00 \end{cases} \qquad (5.11)$$

There were 6 different materials that could be selected based on the value of h', which can be seen in Table 5.2.

CT range (h')	Material	Identity Number
0.00 - 0.08	AIR700ICRU	1
0.08 – 0.60	LUNG700ICRU	2
0.60 – 0.98	TISSUE700ICRU	3
0.98 – 1.01	H2O700ICRU	4*
1.01 – 1.10	TISSUE700ICRU	3
1.10 – 3.00	ICRPBONE700ICRU	5
> 3.00	STL316	6

*Table 5.2: List of the materials used in the Monte Carlo calculations for the water tank containing the steel rod. *A narrow range of CT numbers was set to water for calibration purposes.*

Note that five of the six materials are defined as per the 700ICRU PEGS4 (EGSnrc pre-processor) data file published with the codes [36]. The last material, labeled STL316, was generated using PEGS. The physical characteristics used to define it were obtained directly from the manufacturer of the steel rod used in the measurements.

Voxel dimensions were taken from the RT dose file imported from Eclipse and were set

to 0.25 x 0.25 x 0.30 cm (Y x X x Z). The grid point locations were also set to coincide with the RT dose grid points. The MVCT images required downsampling however, and interpolation was used. The body structure from the RT structure data set was used as a mask so that all voxels outside this boundary were set to air to minimize artefacts introduced on the outer edges of the MVCT images.

5.2.1.5 Varian Clinac 2100EX Linear Accelerator

The 2100EX Clinac is a clinical linear accelerator used for external beam radiotherapy. It can produce photon beams of 6 or 15MV, as well as electron beams of 6, 9, 12, 15 and 18 MeV.

5.2.1.6 TomoTherapy HI·ART II delivery system

Details of the TomoTherapy system may be found in 3.2.1.1.

5.2.2 Dose Measurement

The Clinac 2300EX linear accelerator provided a 15 MV 8×8 cm^2 beam which entered the tank through one of the Plexiglas walls with a source-to-surface distance of 72.4 cm. Nineteen dose profiles were measured at 1 cm intervals behind the steel rod, with the first profile located as close as possible to the rod (a distance of 1.3 cm to the rod edge) and the last profile located 19.3 cm behind it. Each scan was 20 cm in length extending roughly 10 cm above the center of the rod and 10 cm below it as shown in Figure 5.2. A millimetre ruler was used to ascertain the depth of the ion chamber in the tank at the position closest to the rod.

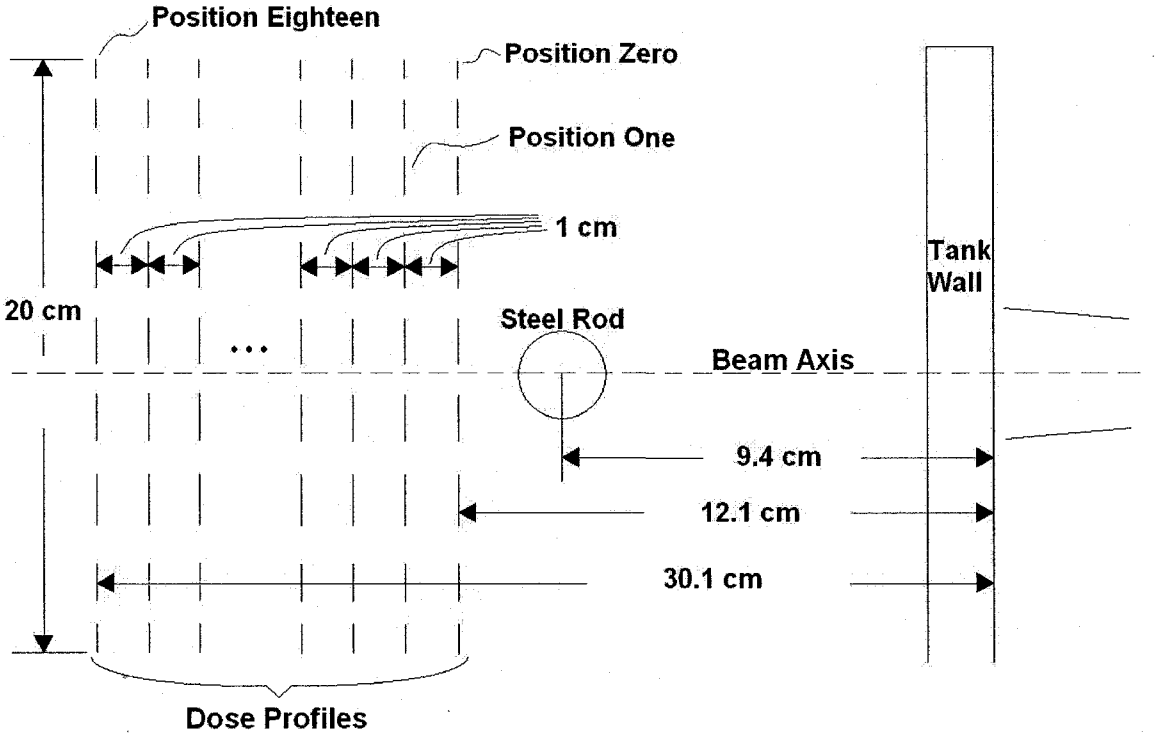

Figure 5.2: Cutaway view of the water tank used in measurements showing the plane containing the beam axis and perpendicular to the axis of the metal rod.

The scans mapping out the dose distribution behind the metal rod were measured using a CC13 ion chamber (Scanditronix Wellhofer North America, Bartlett, TN) and the Wellhofer electrometer.

The Blue Phantom is used for relative dose measurements in our clinic and therefore has not been calibrated for absolute dosimetry. As such, it was necessary to take extra measurements so that the profiles obtained using the Blue Phantom could be compared properly to calculated plans from Eclipse and Monte Carlo. A series of open field measurements were taken in order to facilitate this comparison. The setup and sampling locations were identical to those described above, but with the steel rod removed. The number of monitor units delivered at each measurement point in the measurement setup was unknown due to the continual motion of the ionisation chamber. The calibration consists of comparing open field measurements to open field calculations to find the multiplicative factor which would account for the difference in monitor units delivered

in each case and bring open field measurements and calculations into agreement. This factor would then be used in the comparison of the measurements with the steel rod present.

Open Field Agreement

This method assumes that both the Eclipse TPS and the Monte Carlo system are able to predict the dose distribution of an open field accurately. A sample comparison of Eclipse calculations to measurement can be seen in Figure 5.3 and Figure 5.4 for a field size of 10 x 10 cm^2 and a depth of 20cm. The Eclipse commissioning data was available for 6x6 cm^2 and 10x10 cm^2 fields and the largest relative difference between calculation and measurement in the open field (not including penumbra) was 0.7%. We assume that agreement for an 8x8 cm^2 field is similar. Comparisons were made at depths of 3, 5, 10, 20 and 30 cm. Comparisons of Monte Carlo calculations to measurements are shown in Figure 5.5. Dose profiles taken both on and off axis are shown and all profiles had 90% of points in agreement to within 2% in terms of dose or 2 mm in terms of distance.

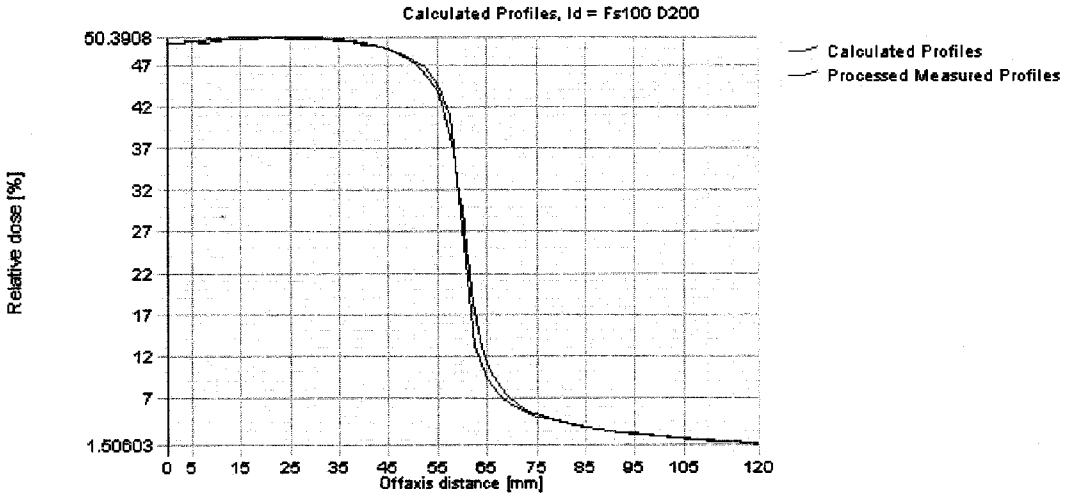

Figure 5.3: A comparison of calculated and measured beam profiles for a 10x10 cm^2 field at a depth of 20cm in a water tank. The processed measured profiles were dose measurements imported into Eclipse, which processed the data in order to characterize the linear accelerator. The calculated profiles are Eclipse calculations carried out in a water phantom.

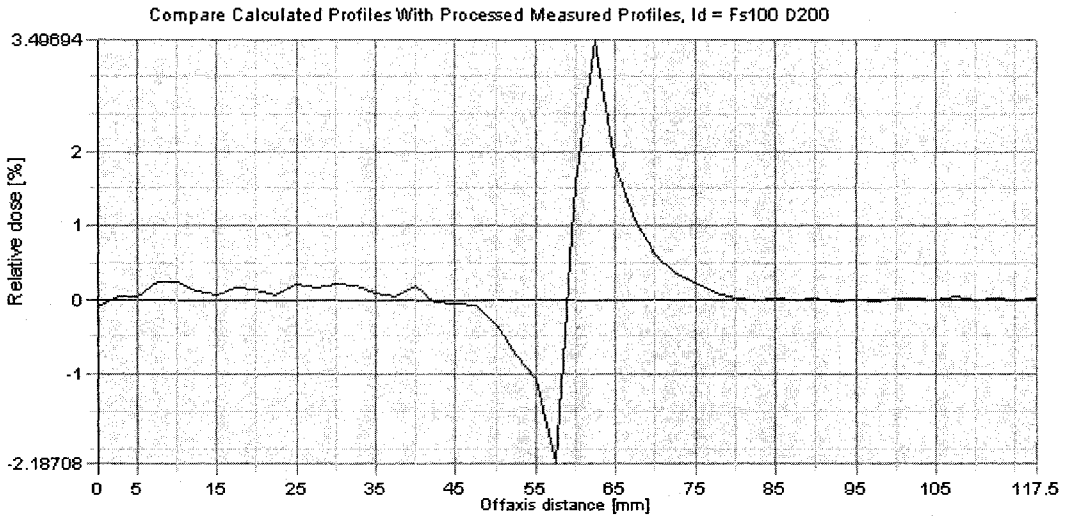

Figure 5.4: The relative dose difference as a function of off axis distance. Note that in the region we are interested in (away from the penumbra) the agreement is within 0.7% for 6 × 6 cm^2 and 10 × 10 cm^2 fields.

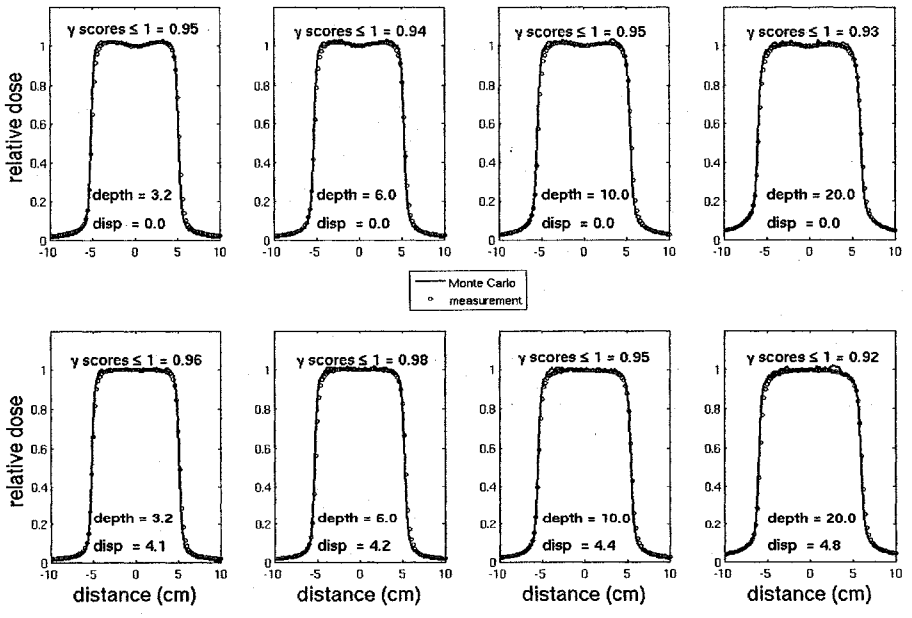

Figure 5.5: Results of comparisons between EGSnrc Monte Carlo calculations and measurement for a 15MV 10×10 cm^2 field at four different depths both on axis and displaced. The γ scores indicate the fraction of points which meet the 2%/2mm acceptance criterion.

5.2.3 Dose Calculation with the Eclipse TPS

The Eclipse treatment planning system with the AAA algorithm (v 7.5.18 & v 8.0.5) was used to calculate dose distributions for comparison with measurement. Details about the Eclipse TPS and the AAA algorithm may be found in 4.2.1.1.

An in-house water tank containing the stainless steel rod and holder was scanned in the TomoTherapy HI·ART II unit in imaging mode and imported into Eclipse for treatment planning. The Scanditronix Wellhofer tank could not be used because it was too large to fit into the HI·ART II bore. Using Eclipse, a treatment identical in geometry to the one delivered for measurements was planned on the MVCT images of the tank. A single fraction of 200 cGy was planned to be delivered to isocentre. The dose was then calculated using both versions of the AAA algorithm. Dose profiles were extracted from the calculated dose distributions for comparison with measured dose profiles.

The image set was then duplicated, and the average CT number for the water in the tank was found using Eclipse contouring tools. The metal rod was then eliminated from the MVCT image by outlining the rod and the region around it and assigning CT numbers equal to the average water CT number. A beam setup identical to the measurement setup and previous calculations was then applied to the tank, and the dose was calculated. Beam profiles were again extracted from the calculated dose distributions for comparison with measured open field dose profiles.

5.3 Results and Discussion

5.3.1 Open Field Calibration

Using the calculated open field profiles (i.e. with no metal rod) and the measured open field profiles, the multiplicative conversion factor needed to compare all subsequent measurements could be found as follows. The average dose in each profile was found for a 4cm portion of the profile centred on the beam axis for both Eclipse calculations and measurements at all depths. The ratio of average calculated dose to average measured dose at each depth was found. Average doses were used to suppress the influence of statistical noise in the measured data. The average ratio of average doses

was found to be 2.132 ± 0.004. All measured doses were scaled using this value in subsequent comparisons between measured and calculated doses. Comparisons of the calculated and scaled measured open fields at various depths can be seen in Figure 5.6. The lateral shift between measured and calculated profiles, visible in both sets of comparisons (ie open field and steel rod) was likely the result of imperfect alignment of the beam axis with the axis of the steel rod during measurement. This was accomplished by aligning the room lasers to the axis of the steel rod, which were difficult to see due to the attenuation of the water in the tank and the reflective surface of the metal.

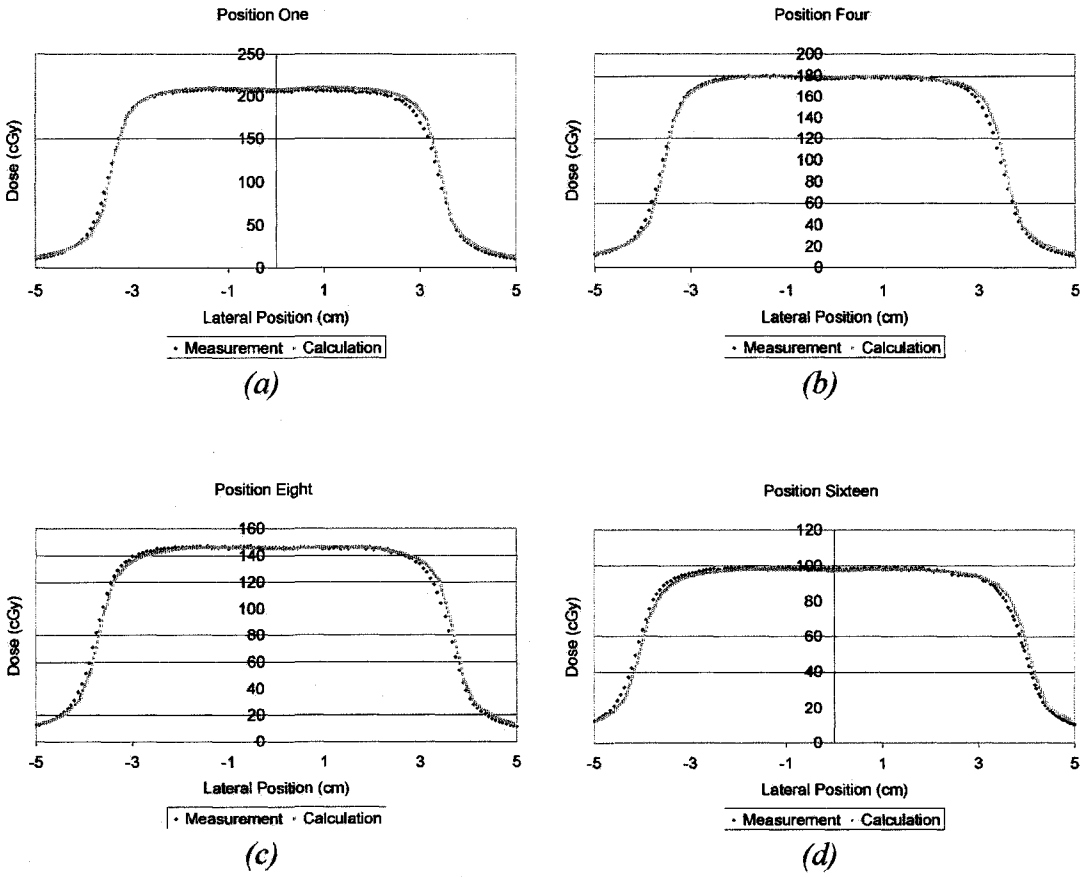

Figure 5.6: Comparison of dose profiles calculated with the AAA algorithm to measurements for an open field.

5.3.2 Comparison of Dose Distributions behind Steel Rod

Comparisons of the dose distributions measured and calculated for a 15MV beam traveling through the stainless steel 316L rod can be seen in Figure 5.7. It should be noted that all Eclipse results shown are for AAA algorithm version 7.5.18. The figures represent the dose profiles measured or calculated at the positions indicated. It is immediately apparent that compared to measurement, Eclipse overestimates the dose delivered behind the rod at all depths despite having accurate electron density information provided by the MVCT scans. This overestimation generally increases with depth from a minimum of 9.9% at the position closest to the rod to a maximum of 20.0% at the position furthest from the rod. Differences between Monte Carlo calculations and measurement on the other hand range from a minimum of 0.08% to a maximum of 4.1% and there is no simple correlation with depth. This is more clearly seen in Figure 5.8, where the absolute and relative local differences in cGy and percent between measurement and calculations have been plotted for various depths. The local difference is calculated using:

$$\Delta D = \left[\frac{D_{measured} - D_{calculated}}{D_{measured}} \right] \times 100\% \qquad (5.13)$$

There are two possible explanations for the overestimation of dose predicted by Eclipse. Either Eclipse is overestimating the primary dose by underestimating the attenuation of the metal rod, or it is overestimating the scattered dose behind the rod. Underestimation of the attenuation of high density materials could occur if 1) CT numbers used by Eclipse are capped, 2) if electron densities themselves are being capped, as was the case for Ding et al or 3) if the inhomogeneity correction algorithm for high density materials is incorrect. We manually capped the CT numbers of the plug at various values using contouring tools in the Eclipse TPS to see if we could reproduce the underestimation and failed. We also manually capped the electron densities by using truncated CT number – to – electron density calibration curves and failed to reproduce the underestimation. The third possibility could be investigated by separating primary contributions from scatter contributions by manually inserting objects of very high

electron density into CT images, effectively eliminating primary dose contributions to points behind the object. Eclipse dose calculations could then be compared to Monte Carlo simulations to get a better understanding of how primary dose calculations and scattered dose contributions are handled by the Eclipse algorithm. Such calculations are beyond the scope of this thesis.

A recalculation of the dose distribution using the latest version of the AAA algorithm (v 8.0.5) produced a distribution identical to the original calculation (v 7.5.18).

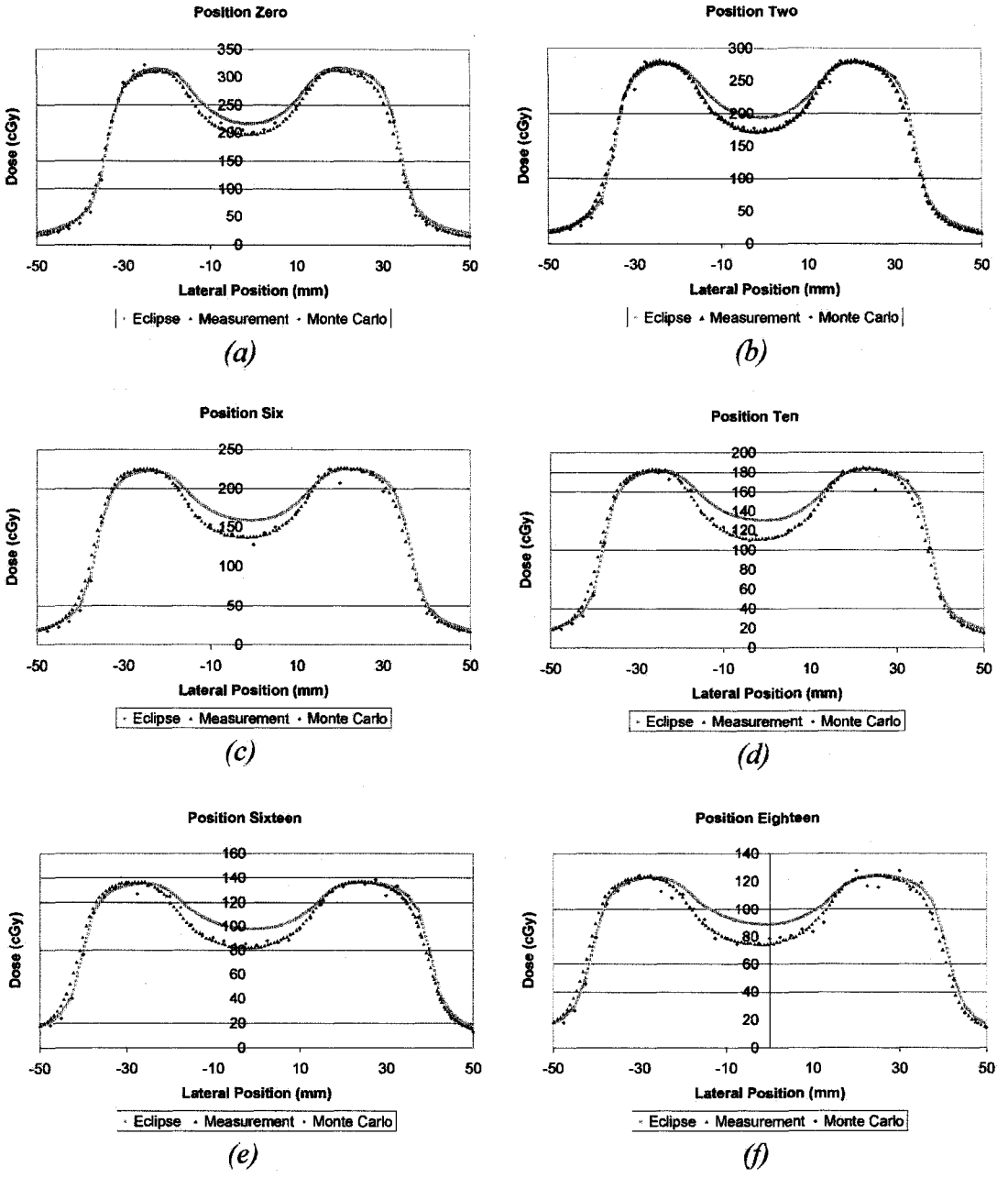

Figure 5.7: Dose profiles taken perpendicular to the beam axis at different depths in the tank. The depth of each measurement behind the metal rod is the position number plus 1.3cm.

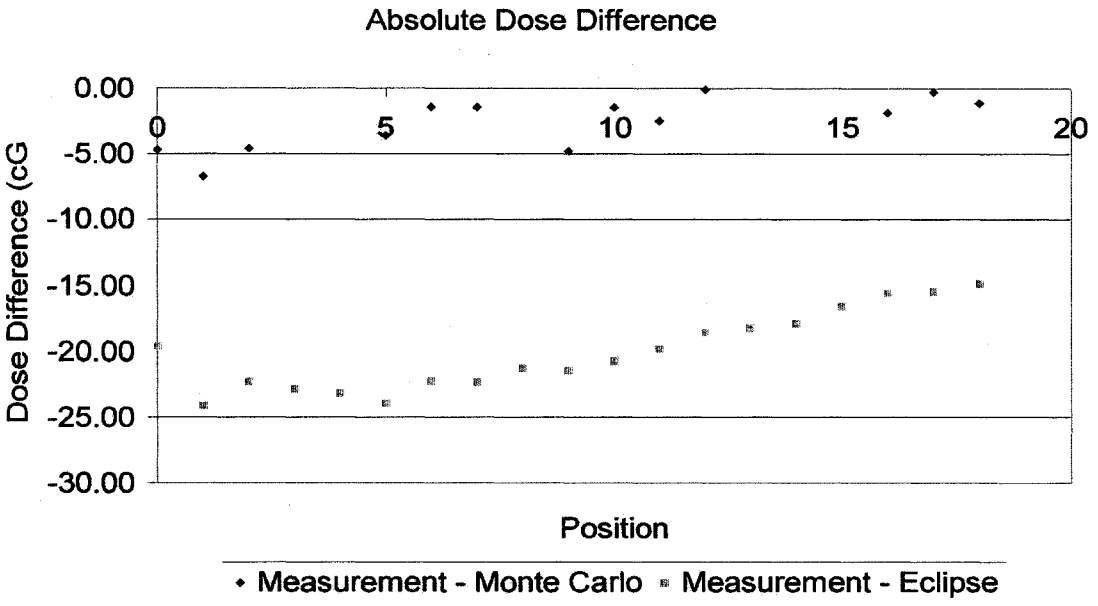

(a)

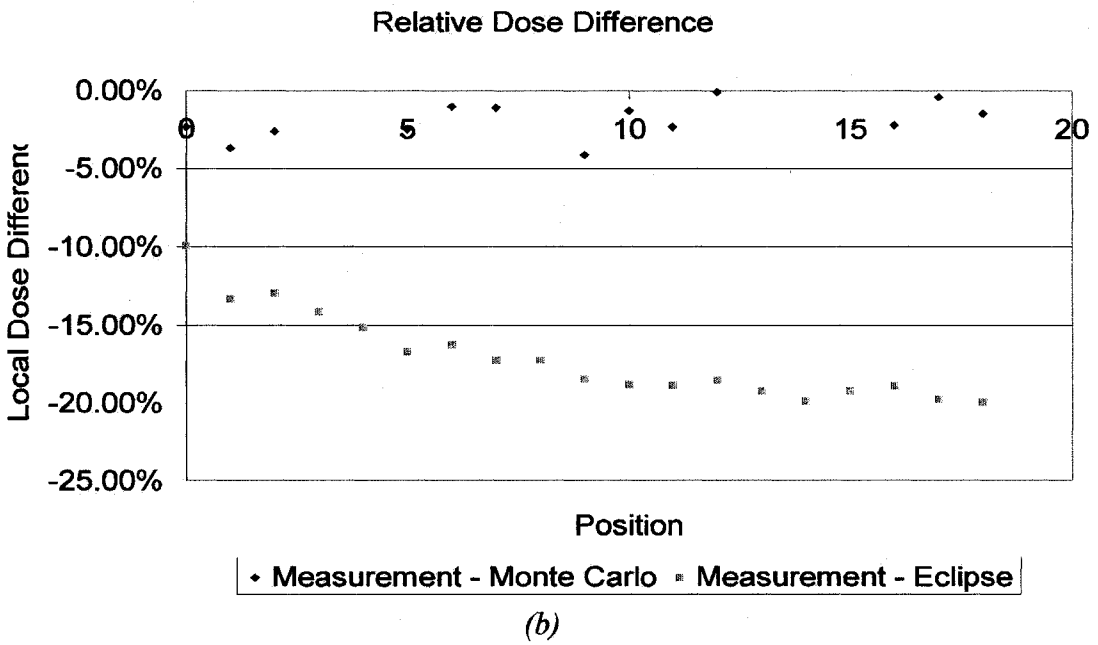

(b)

Figure 5.8: Difference in minimum dose behind steel rod measured and minimum dose calculated. Numbers shown are measurement minus calculation. The depth of each measurement behind the metal rod is the position number plus 1.3cm.

The underestimation of dose distal to a metal implant from 9.95% to 20% limits the usefulness of using MVCT with its improved electron density information because the high electron density information appears not to be correctly used by the AAA dose calculation algorithm. It is clear that the problem lies with the treatment planning system as opposed to the MVCT number-to-electron density calibration or the MVCT images, as the Monte Carlo calculations agree well with measurement using the same image sets and calibration.

Chapter 6: Final Discussion and Conclusions

6.1 Summary of Results

6.1.1 CT Number to Electron Density Calibration

Our measurements show that the MVCT number-to-electron density calibration is stable. CT values for tissue equivalent and metal plugs were not significantly affected by plug depth or location with respect to the bore axis, except in three cases where the average CT value measured for a particular plug in a particular arrangement was not the same as the average CT values for that plug in other plug arrangements to within the experimental error. Two of the three discrepancies that were identified were influenced by the presence of a metal artifact directly overlapping the plugs. The third discrepancy occurs for lead, which is dense enough to cause significant beam hardening. Its CT number was therefore influenced by its depth in the phantom to the point where values measured for two different depths were not the same to within the experimental error. Since lead is much denser than the metals and alloys used in hip implants (~ 1.44 times denser than steel in terms of mass) this is not a clinically significant shortcoming.

The images used to perform the MVCT calibration also demonstrated the superior resilience of MVCT numbers to the presence of metal artifacts. For the four plugs affected by the presence of metal artifacts, the increase in the standard deviation of the mean and the change in the value of the mean was larger for kVCT images in all cases. When converted to changes in relative electron density, the performance of the kVCT images was equal to the MVCT images in the best case, and far inferior in the worst with a measured relative electron density change 21 times larger than in the MVCT images. For the two other cases, the measured relative electron density change was 2 x and roughly 6 x larger for the kVCT images than the MVCT images. kVCT numbers for metals were also found to be highly inaccurate due to saturation, with the average numbers for the four different metals equal to within error, despite a density difference

of roughly a factor of 4 between Pb and Al. Average MVCT numbers on the other hand remained well spaced, with much smaller standard deviations, and equal to their theoretical values within error.

6.1.2 Clinical Impact of Metal Artifacts

The results of our assessment of the use of MVCT for contouring prostates for patients with hip implants was inconclusive, but hinted at the superiority of kVCT images for contouring the prostate, especially for patients with single hip implants. This is due to the increased noise and decreased contrast inherent to MVCT imaging negating the potential benefit of decreased metal artifacts that it offers. With only four patients from which to make a conclusion however, this area requires further study. Furthermore, there is room for improvement of the MVCT images, in particular in the improvement of the detectors used in the system, which may turn the tables in favour of MVCT.

Our assessment of the differences in dose distributions predicted using MVCT and kVCT images showed that the clinical benefit offered by using MVCT images in conjunction with the Eclipse TPS was marginal. In the shadow of the metal implant, there difference in dose predicted between the two imaging modalities was roughly 1.4%, despite the fact that the electron density used in the calculation was approximately 3 times as high in the MVCT images.

6.1.3 Dose Calculation Accuracy with Metal Implants

The comparison of Eclipse AAA calculations to measurement and Monte Carlo conclusively demonstrated the inability of the AAA algorithm to accurately calculate dose behind a steel inhomogeneity. Measurements demonstrated that both versions of the algorithm available clinically overestimate the local dose behind the rod anywhere from 10% to 20% of measurements, whereas Monte Carlo calculations agreed with measurements to within roughly 4%. For comparison, Lin et al found that the ADAC/Pinnacle^3 algorithm could predict the dose away from the buildup region to within 4-5% of Monte Carlo simulations [43]. This presents difficulties for the clinical implementation of this work, as the advantage of accurate CT numbers in the presence

of metal artifacts offered by MVCT imaging is offset by the inability of the AAA dose calculation algorithm to calculate the dose properly. Until the dose calculation algorithm is improved, there would be little point in pursuing this course further, as the main purpose was to make the treatment planning process for patients with metal implants as simple as for those without.

It is worth while noting again that the use of MVCT imaging still offers potential benefits for patients with metal implants. In our clinic however, these benefits are offset by the shortcomings of the dose calculation algorithm in use currently and for the foreseeable future.

6.2 Future Work

Once a more robust dose calculation algorithm is available, the potential benefit of the use of MVCT for planning hip prosthesis patients may be assessed. This would be possible by comparing treatment plans generated using both kVCT and MVCT image sets for calculations in a TPS and examining the differences between the two. The image sets used for the contouring comparisons in 4.2.1.2 can be used for this purpose. Treatment plans could also be generated using Monte Carlo dose calculations for both kVCT and MVCT image sets in order to eliminate the error introduced by using current commercial dose calculation algorithms. Different clinically useful beam arrangements could be used, which would help identify when the use of MVCT imaging is required, and when kVCT images would suffice.

This work may also be easily extended to different sites, provided that kVCT and MVCT image sets of other typical implant sites are available (eg head and neck with dental fillings). The findings of this work are for the prostate only, since the extent to which artifacts affect images and dose calculations will depend on the size of the metal implant and its proximity to the region of interest. This will change from site to site.

6.3 Final Conclusions

The use of MVCT imaging in treatment planning offers definite advantages and disadvantages for patients with metal hip prostheses. Metal artifacts are suppressed, and the CT numbers of regions affected by artifacts, and the associated electron densities, are therefore more representative of the actual values. Our measurements demonstrated that the change in apparent electron density can be as much as 21 times smaller if MVCT is used. This implies more accurate information for treatment planning. The MVCT modality suffers from higher noise and lower contrast than kVCT imaging however, offsetting the potential benefit of reduced metal artifacts. Whether MVCT or kVCT is the preferred modality will therefore depend strongly on the extent to which metal artifacts affect regions of interest, and therefore on the site and the number, size and type of the implants. Improvements in algorithms for reducing metal artifacts may limit the advantage of MVCT images in the future.

The MVCT number-to-electron density calibration curve is not dependent on plug or phantom arrangement and can be easily measured and used in treatment planning calculations. Neither plug depth nor phantom position inside the MVCT bore had a noticeable effect on the measured CT number. Since the electron densities of the metal implant itself and surrounding regions affected by metal artifacts are more representative of the true value, the use of MVCT for dose calculations in the presence of metal artifacts should be more accurate in theory. The choice of dose calculation algorithm will determine the extent to which this is true in practice. In our case the Eclipse AAA algorithm overestimated the dose behind a metal rod anywhere from 10% to 20% of the local dose. Monte Carlo on the other hand agreed with measurements to within roughly 4%. This limits the potential benefit offered by the use of MVCT for treatment planning for patients with metal implants, and prevents us from simplifying the treatment planning process for these patients. This may be rectified in the future by the use of a dose calculation algorithm capable of handling calculations in the presence of metal more accurately, at which time the clinical benefits of the use of MVCT will be worth assessing as the simplification of treatment planning will be realizable.

Glossary of Acronyms and Symbols

3DCRT	Three Dimensional Computed Radiation Therapy
AAA	Anisotropic Analytical Algorithm
AAPM	American Association of Physicists in Medicine
CSDA	Continuous Slowing Down Approximation
CT	Computed Tomography
CTV	Clinical Target Volume
DICOM	Digital Imaging and Communications in Medicine
DICOM RT	Digital Imaging and Communications in Medicine - Radiotherapy
EPID	Electronic Portal Imaging Device
GTV	Gross Tumour Volume
HI·ART	Highly Integrated Adaptive Radiation Therapy
HU	Hounsfield Unit
ICRU	International Commission on Radiation Units and Measurements
IGAR	Image Guided Adaptive Radiotherapy
IMRT	Intensity Modulated Radiotherapy
IV	Irradiated Volume
kVCT	Kilovoltage Computed Tomography
MC	Monte Carlo
MR	Magnetic Resonance
MRI	Magnetic Resonance Imaging
MVCT	Megavoltage Computed Tomography
NIST	National Institute of Standards and Technology
OAR	Organ At Risk
PET	Positron Emission Tomography
PSF	Point Spread Function
PTV	Planning Target Volume
R^2	Pearson product-moment correlation coefficient
ROI	Region Of Interest
SPECT	Single Photon Emission Computed Tomography
TPS	Treatment Planning System
TV	Treated Volume
XCOM	Photon Cross Sections Database
Z	Atomic Number
$\lambda(\varphi, x)$	Radon transform of an object distribution
μ	Attenuation Coefficient
μ/ρ	Mass Attenuation Coefficient
ρ	Density

Bibliography

1: A C Kak and M Slaney, **Principles of Computerized Tomographic Imaging**. 345 East 47th Street, New York, NY: The Institute of Electrical and Electronics Engineers, Inc., 1988.

2: "cancer" , **Webster's Dictionary**, Ashland, Ohio: Landoll, 1993.

3: **What is cancer?**, Canadian Cancer Society, December 14 2006, <http://cancer.ca/ccs/internet/standard/0,3182,3172_562847522__langId-en,00.html>.

4: **Chronic Disease Clock Explanation**, Centre for Chronic Disease Prevention and Control, April 12 2005, <http://www.phac-aspc.gc.ca/ccdpc-cpcmc/footnote_e.html>.

5: **General cancer stats for 2007**, Canadian Cancer Society, April 11 2007, <http://www.cancer.ca/ccs/internet/standard/0,2283,3172_14423__langId-en,00.html>.

6: **Canadian Cancer Statistics 2007**, Canadian Cancer Society/National Cancer Institute of Canada, April 11 2007, <http://www.cancer.ca/ccs/internet/standard/0,2283,3172_14423__langId-en,00.html>.

7: **Prostate Cancer, Canadian Cancer Encyclopedia**, Canadian Cancer Society, May 18 2007, <http://info.cancer.ca/E/CCE/cceexplorer.asp?tocid=41>.

8: **Radiation Oncology Services**, United States Department of Veterans Affairs, 2005, <http://www1.va.gov/ntxradoncology/page.cfm?pg=2>.

9: A Neal, "Target Definition", Chapter 29, 637 - 646, **Handbook of Radiotherapy Physics: Theory and Practice**. Boca Raton, FL: CRC Press, Taylor and Francis Group, 2007.

10: ICRU (International Commission on Radiation Units and Measurements), Prescribing, recording and reporting photon beam therapy, 1993

11: I A Cunningham and P F Judy, **The Biomedical Engineering Handbook**. Boca Raton, FL: CRC Press, LLC, 2000.

12: S Rathee, "Artifacts in CT Images", Class Notes, Oncology 568: The theory of Medical Imaging, Cross Cancer Institute, University of Alberta, 2005

13: J Wei, L Chen, G Sandison, Y Liang and L Xu, "X-ray CT high-density artefact suppression in the presence of bones", Phys. Med. Biol. *49*, 5407-5418 (2004).

14: A Mahnken, R Raupach, J Wildberger, B Jung N Heussen, T Flohr, R Gunther and S Schaller, "A New Algorithm for Metal Artifact Reduction in Computed Tomography", Invest. Radiol. *38*, 769-775 (2003).

15: M Yazdia, L Gingras and L Beaulieu, "An Adaptive Approach To Metal Artifact Reduction In Helical Computed Tomography For Radiation Therapy Treatment Planning: Experimental and Clinical Studies", Int. J. Radiation Oncology Biol. Phys. *4*, 1224-1231 (2005).

16: C Reft, R Alecu, I Das, B Gerbi, P Keall, E Lief, B Mijnheer, N Papanikolaou, C Sibata and J Van Dyk, , "Dosimetric considerations for patients with HIP prostheses undergoing pelvic irradiation. Report of the AAPM Radiation Therapy Committee Task Group 63", Med. Phys. *6*, 1162-1182 (2003).

17: **Hip Replacement**, Wikipedia, October 2007, <http://en.wikipedia.org/wiki/Hip_implant>.

18: M Bal and L Spies, "Metal artifact reduction in CT using tissue-class modeling and adaptive prefiltering", Med. Phys. *8*, 2852-2859 (2006).

19: D Xia, J Roeske, L Yu, C Pelizzari, A Mundt and X Pan, "A hybrid approach to reducing computed tomography metal artifacts in intracavitary brachytherapy", Brachytherapy , 18-23 (2005).

20: J Roeske, C Lund, C Pelizzari, X Pan and A Mundt, "Reduction of computed tomography metal artifacts due to the Fletcher-Suit applicator in gynecology patients receiving intracavitary brachytherapy", Brachytherapy , 207-214 (2003).

21: L Schreiner, A Kerr, G Salomons, C Dyck and G Hajdok , "The Potential for Image Guided Radiation Therapy with Cobalt-60 Tomotherapy", Chapter , 449-456, **Medical Image Computing and Computer-Assisted Intervention - MICCAI 2003**. : Springer Berlin / Heidelberg, 2003.

22: T Mackie, J Balog, K Ruchala, D Shepard, S Aldridge, E Fitchard, P Rechwerdt, G Olivera, T McNutt and M Mehta, "Tomotherapy", Semin Radiat Oncol *1*, 108-117 (1999).

23: K Langen, S Meeks, D Poole, T Wagner, T Willoughby, P Kupelian, K Ruchala, J Haimerl and G Olivera, "The use of megavoltage CT (MVCT) images for dose recomputations", Phys. Med. Biol. , 4259-4276 (2005).

24: K Ruchala, G Olivera, E Schloesser and T Mackie, "Megavoltage CT on a tomotherapy system", Phys. Med. Biol. , 2597-2621 (1999).

25: H Johns and J Cunningham, **The Physics of Radiology**. Springfield, Illinois: Clarence C Thomas, 1983.

26: J Rosenwald, I Rosenberg and G Shentall, "Patient Dose Computation For Photon Beams", Chapter 26, 559-586, **Handbook of Radiotherapy Physics: Theory and Practice**. Boca Raton, FL: CRC Press, Taylor & Francis Group, 2007.

27: A Nahum, "Monte-Carlo Based Patient Dose Computation", Chapter 28, 603-620, **Handbook of Radiotherapy Physics: Theory and Practice**. Boca Raton, FL: CRC Press, Taylor & Francis Group LLC, 2007.

28: A Bielajew, "The Monte Carlo Simulation of Radiation Transport", Chapter 5, 75-88, **Handbook of Radiotherapy Physics**. Boca Raton, FL: CRC Press, Taylor & Francis Group LLC, 2007.

29: K J Ruchala, G H Olivera, E A Schloesser, R Hinderer and T R Mackie, "Calibration of a tomotherapeutic MVCT system", Phys. Med. Biol. *45*, N27-N36 (2000).

30: **ImageJ**, National Institutes of Health, 1997-2007, <http://rsb.info.nih.gov/ij/>.

31: **XCOM: Photon Cross Sections Database**, National Institute of Standards and Technology, August 2005, <http://physics.nist.gov/PhysRefData/Xcom/Text/XCOM.html>.

32: A Fogliata, G Nicolini, E Vanetti, A Clivio and L Cozzi, "Dosimetric validation of the anisotropic analytical algorithm for photon dose calculation: fundamental characterization in water", Physics in Medicine and Biology *51*, 1421-1438 (2006).

33: T Moller and E Reef, **Pocket Atlas of Cross Sectional Anatomy, Computed Tomography and Magnetic Resonance Imaging**. : Thieme Medical Publisher Inc., New York, 1994.

34: G Ding and C Yu, "A Study on Beams Passing Through Hip Prosthesis for Pelvic Radiation Treatment", Int. J. Radiation Oncology Biol. Phys. *4*, 1167-1175 (2001).

35: Wellhofer Dosimetrie GmbH, Blue Phantom Manual, 2001

36: I Kawrakow and D Rogers, The EGSnrc Code System: Monte Carlo Simulation of Electron and Photon Transport, NRCC Report PIRS-701, 2003

37: D Rogers, B Faddegan, G Ding, C Ma, J We and T Mackie, "BEAM: a Monte Carlo code to simulate radiotherapy treatment units", Med Phys *5*, 503-524 (1995).

38: D Rogers, B Walters and I Kawrakow, BEAMnrc Users Manual NRCC Report PIRS-0509(A)rev I, 2005

39: B Walters, I Kawrakow and D Rogers, DOSXYZnrc Users Manual NRCC Report PIRS-794rev B, 2005

40: D Sheikh-Bagheri and D Rogers, "Sensitivity of megavoltage photon beam Monte Carlo simulations to electron beam and other parameters", Med Phys *3*, 379-390 (2002).

41: I Popescu, C Shaw, S Zavgorodni and W Beckham, "Absolute dose calculations for Monte Carlo simulations of radiotherapy beams", Phys Med Biol *14*, 3375-3392 (2005).

42: I Kawrakow, M Fippel and K Friedrich, "3D electron dose calculation using a Voxel based Monte Carlo algorithm (VMC)", Med Phys *4*, 445-457 (1996).

43: S Lin, T Chu, J Lin and M Liu, "The effect of a metal hip prosthesis on the radiation dose in therapeutic photon beam irradiations", Applied Radiation and Isotopes *57*, 17-23 (2002).